Contents lists available at ScienceDirect

# **Tectonophysics**

journal homepage: www.elsevier.com/locate/tecto



# The 2020 Qotur earthquake doublet and its implication for the geodynamics of Northwestern Iran

Abdolreza Ghods <sup>a,\*</sup>, Mahin Jafari <sup>a</sup>, Jochen Braunmiller <sup>b</sup>, Mahtab Aflaki <sup>a</sup>, Eric Bergman <sup>c</sup>, Zahra Mousavi <sup>a</sup>, Esmaeil Farzaneghan <sup>d</sup>, Andrea Walpersdorf <sup>e</sup>

- <sup>a</sup> Department of Earth Sciences, Institute for Advanced Studies in Basic Sciences, Zanjan, Iran
- <sup>b</sup> School of Geosciences, University of South Florida, Tampa, FL, USA
- Global Seismological Services, Golden, CO, USA
- <sup>d</sup> Road, Housing and Urban Development Research Center, Building and Housing Research Network, Tehran, Iran
- e Univ. Grenoble Alpes, CNRS, IRD, UGE, ISTerre, Grenoble, France

#### ARTICLE INFO

# Keywords: Qotur earthquake doublet Zagros main recent fault Bashkale fault system Transtensional stress regime InSAR modeling Earthquake relocation Stress inversion

### ABSTRACT

The 23 February 2020 Qotur earthquake doublet (5.7 and 5.9  $M_{\rm w}$ ) occurred near the Iran-Turkey border. The doublet ruptured along the northern segment of the Bashkale fault system, which forms the northernmost end of the Zagros' Main Recent Fault. To investigate the tectonics of the region, we combined geological fault mapping, precise location of the seismic cluster, moment tensors of the mainshocks and 28 larger fore- and aftershocks, InSAR source modeling, and inversion of source parameters for the regional stress field. We show that both mainshocks happened on NE-SW trending left-lateral strike-slip faults belonging to the Bashkale fault system. However, both NE-SW trending left-lateral and NW-SE trending right-lateral strike-slip faults were activated by the earthquake cluster. The InSAR images imply no surface rupture for the doublet event in agreement with the field observations. The first mainshock was deeper (centroid: 9 km) than the second mainshock (5 km). We model the InSAR data of the second mainshock as rupture along a 7-km-wide and 5-km-long fault with maximum displacement of 1.2 m at ~3 km depth. The spatial distribution of aftershocks and the damaged region implies southwest directivity for the second mainshock. Stress inversion of the moment tensors indicates a transtensional regime with an NNW-SSE direction of maximum horizontal stress. This agrees with the stress regime deduced from the inversion of geologically measured fault planes and GPS vectors, and the focal mechanism of the 1930 Salmas earthquake. Our results show that strain accommodation at the northern end of the right-lateral strikeslip Main Recent Fault of the Zagros is distributed across a complex network of immature conjugate right and left-lateral strike-slip and normal faults.

#### 1. Introduction

The Qotur earthquake doublet happened on 23 February 2020 in a mountainous region  $\sim\!45$  km southwest of the city of Khoy and  $\sim\!40$  km northwest of Salmas in the West Azerbaijan province of Iran near the Iran-Turkey border (Fig. 1). The doublet also has been named the Qotur-Ravian doublet (Taymaz et al., 2022). The first main event with a magnitude of 5.8  $M_{ww}$  (USGS) happened at 5:52 UTC (9:22 AM local time) followed by a second main event of magnitude 6.0  $M_{ww}$  (USGS) at 16:00 UTC (7:30 PM local time). The second event inflicted most of the building damages. Except for some minor NE-SW trending fissures on asphalted roads, no surface rupture has been reported for the doublet

event (Esmaeili et al., 2020). The doublet was preceded by a 10-day long foreshock sequence with the largest foreshock reaching magnitude 4.5  $M_{\rm w}$  on February 16. The doublet was followed by 18  $M_{\rm w} \geq$  4.0 aftershocks up to the end of May 2020. The doublet caused about 110 injuries in Iran, and about ten fatalities and 66 injuries, mostly in the Ozpinar village (Fig. 1b) in the Bashkale district of the Van region, Turkey (Taymaz et al., 2022). The epicenter of the second main event was close to Zari village and Qotur city but the most serious damages to Iranian (Esmaeili et al., 2020) and Turkish villages were reported from towns southwest of the epicenter near the Iran-Turkey border (Taymaz et al., 2022). The maximum observed intensity of the Qotur doublet in Iran was VII on the modified Mercalli scale (Fig. 2) (Esmaeili et al., 2020).

E-mail address: aghods@iasbs.ac.ir (A. Ghods).

<sup>\*</sup> Corresponding author.

Seismicity in NW Iran is mostly concentrated on the right-lateral North Tabriz-Gailatu (NTG) fault system to the north and east of the study area. However, the largest instrumentally recorded event in NW Iran is the 1930 Salmas 7.1  $\rm M_w$  (Storchak et al., 2013 and 2015; Di Giacomo et al., 2018) event which happened south of the NTG, along the NW-SE trending oblique  $\sim\!40\text{-km-long}$  Salmas fault (Fig. 1b). The 1930 Salmas event involved mostly right-lateral surface faulting and minor secondary left-lateral faulting on the NE-SW trending Derik fault (Berberian and Tchalenko, 1976).

The Qotur doublet happened in the northern part of the complex Serow-Bashkale fault system (Niassarifard et al., 2021), south of the NW- SE trending NTG fault system and west of the Salmas macroseismic zone (Fig. 1). The Serow-Bashkale fault system lies in the northern part of the Zagros Main Recent Fault (MRF). The MRF exhibits fault-parallel strain rates of 1–2 mm/yr (e.g., Watson et al., 2024) but the rather sparse GPS data in the study area (Khorrami et al., 2019) suggest a maximum eastwest-directed tensional strain rate of about 1 mm/yr. As a whole, the system causes an eastward mass transport and thus accommodates right-lateral motion of the MRF (Niassarifard et al., 2021). The Qotur doublet provides an exceptional opportunity to investigate how the cross-cutting NE-SW and NW-SE trending faults of the Serow-Bashkale fault system release seismic strain at the northern end of the Zagros MRF. Two

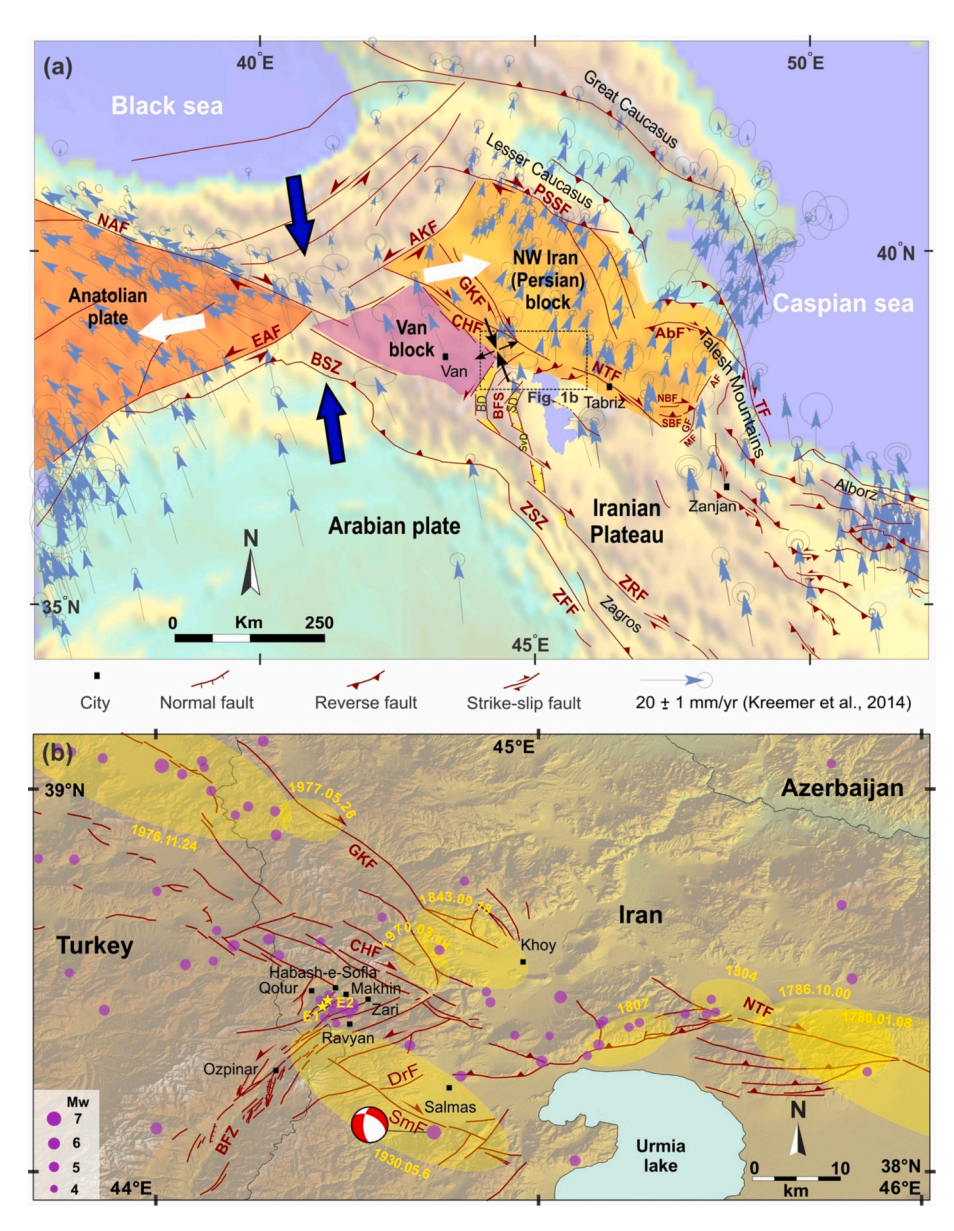


Fig. 1. a) Structural framework of NW Iran and eastern Anatolia, including the major faults and tectonic blocks. Blue GPS velocity vectors (Kreemer et al., 2014; Khorrami et al., 2019) are with respect to fixed Eurasia. The bold blue arrows show the general direction of shortening and the bold white arrows show the direction of the overall mass escape. The black double arrows present the strain axes directions northwest of Urmia Lake from Khorrami et al. (2019). b) Epicenters of the Qotur doublet (yellow stars show main events E1 and E2) together with epicenters of M ≥ 4 earthquakes (purple circles) from the combined ISC-GEM and ISC-EHB earthquake catalogs (spanning 1930–2022), mezoseismal areas of historical earthquakes (yellow ellipse) from Berberian and Yeats (1999) and Karakhanian et al. (2004), as well as major structures are plotted on SRTM 90 m DEM. The red beachball is the focal mechanism of the 1930 Salmas earthquake from the ISC-GEM catalog. Grey lines show the political boundaries. Abbreviations are AF: Ardabil fault, AbF: Arasbaran fault, AKF: Akhurian fault, BFZ: Bashkale fault zone, BSZ: Bitlis suture zone, CHF: Chalderan fault, DrF: Derik fault, EAF: East Anatolian fault, GF: Garmachay fault, GKF: Gailatu-Khoy fault, MF: Mianeh fault, NAF: North Anatolian fault, NBF: North Bozqush fault, NTF: North Tabriz fault, PSSF: Pambak – Sevan – Sunik fault, SBF: South Bozqush fault, TF: Talesh fault, ZFF: Zagros Frontal fault, ZRF: Zagros Main Recent fault, ZSZ: Zagros suture zone, BD: Bashkale depression, SD: Serow depression, SvD: Silvana Depression. (For interpretation of the references to colour in this figure legend, the reader is referred to the web version of this article.)

previous studies derived contradicting right-lateral (Taymaz et al., 2022) and left-lateral (Rezapour, 2024) strike-slip faulting for the doublet. To resolve this issue, we present detailed relocation of the Qotur seismic cluster, 30 moment tensors for larger events in the cluster, and InSAR rupture modeling of the second mainshock. Our multidisciplinary approach aims to derive (1) a high-resolution distributed slip model via combined ascending/descending InSAR, (2) integrate relocated seismicity and focal mechanisms to determine the state of stress, and (3) place the rupture in its broader tectonic context. Our results demonstrate strain accommodation is distributed across conjugate right-and left-lateral strike-slip and normal faults at the northern boundary of the right-lateral strike-slip MRF of the Zagros. This finding has implications for understanding continental deformation processes in young collision zones such as Iran and seismic hazard assessment of NW Iran and NE Turkey.

# 2. Tectonics and active deformation of the area

The Cenozoic tectonic history in the central and western parts of the Iranian plateau is mainly affected by the Arabia-Eurasia convergence with deformation either concentrated along boundaries of the region's micro-blocks or distributed within semi-rigid blocks. In the northern part of the Arabia-Eurasia convergence zone, between longitudes  $36^{\circ}$ - $50^{\circ}$ E and latitudes  $\sim 36^{\circ}$ - $42^{\circ}$ N, deformation is complicated (Fig. 1a). This is due to the interaction of several rigid/semi-rigid plates/blocks including the Arabian and Anatolian plates, the Central Iran microcontinent (plateau), the South Caspian and Black Sea oceanic like blocks, as well as the smaller Persian (or NW Iranian block), Van, and Caucasus blocks. In this region, the  $\sim$ NNW-ward motion of the Arabian plate with respect to fixed Eurasia results in (1) stress partitioning along the northern part of the Zagros suture zone, (2) compressional deformation along the Bitlis suture zone and the Caucasus Mountains, and (3)

nearly eastward escape of the Persian block and westward escape of the Anatolian plate along the deep-seated strike-slip faults bounding the blocks (Vernant et al., 2004; Navabpour and Barrier, 2012; Zarifi et al., 2014; Ghods et al., 2015; Aflaki et al., 2021).

Within the Persian block (Fig. 1a), its ~eastward escape together with the role of the South Caspian Basin as a rigid back-stop results in a compressional/strike-slip stress regime with a NW-SE trending horizontal  $\sigma_1$  stress axis (i.e., Ghods et al., 2015; Afra et al., 2017; Aflaki et al., 2021). Throughout the southern terrain, i.e., Central Iran (Iranian Plateau), the modern regional stress regime is compressional/strike-slip with a NE-SW direction of the  $\sigma_1$  stress axis (e.g., Authemayou et al., 2006; Abdulnaby et al., 2016; Afra et al., 2017; Niassarifard et al., 2021). An exception to a transpressional stress regime is found near the southern border of the Persian block in the area west of Urmia Lake (Fig. 1b) where faulting in the complex Serow-Bashkale fault system reflects a local transfensional stress regime characterized by geologically determined  $\sim$ E-W and  $\sim$  N-S directions of the minimum and maximum horizontal stress axes, respectively (Niassarifard et al., 2021). The fault system consists of crossing NE-SW-trending left-lateral strike-slip faults of the Bashkale fault system and NW-SE-trending right-lateral strike-slip faults such as the Salmas fault, and ~ N-S trending normal faults. The fault system as a whole causes an eastward mass transport in response to the right-lateral motion of the MRF (Niassarifard et al., 2021). The dextral slip along the right-stepping overlapping NW-SE striking northernmost segments of the MRF results in the evolution of pull apart basins, such as the Serow, Silvana and Bashkale depressions (Fig. 1a). The Bashkale depression (Fig. 1b) represents the boundary between the Van block and the Central Iran micro-continent (Niassarifard et al.,

Geological information and earthquake focal mechanisms (e.g., Ghods et al., 2015; Taghipour et al., 2018; Niassarifard et al., 2021) reveal that active deformation in the NW part of the Iranian plateau and

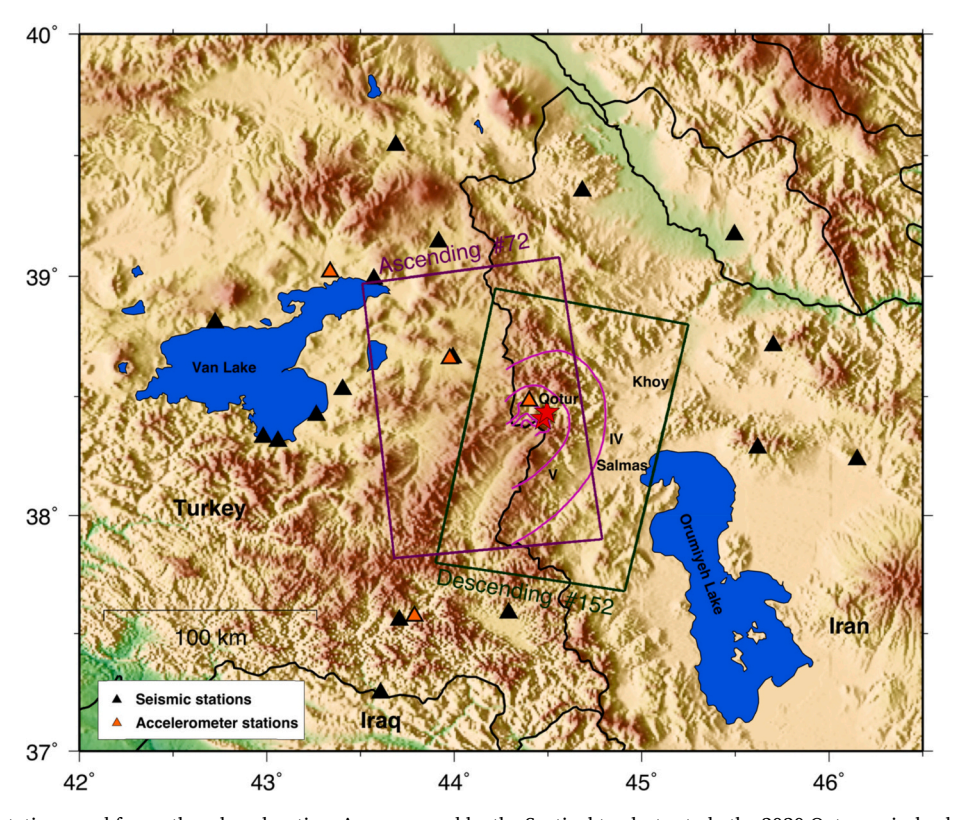


Fig. 2. Regional seismic stations used for earthquake relocation. Areas covered by the Sentinel tracks to study the 2020 Qotur mainshocks (red stars) are shown by black rectangles. Each track is labeled by its track number. Violet curves show the macroseismal region in Iran as reported by Esmaeili et al. (2020); roman numbers (IV and V) show the modified Mercalli intensities. Black lines show the political boundaries. (For interpretation of the references to colour in this figure legend, the reader is referred to the web version of this article.)

east of the Anatolian plateau, is characterized by (1) right-lateral strike-slip faulting along NW-SE striking faults such as the North Tabriz, Chalderan, Gailatu-Khoy, Salmas and North Anatolian faults, (2) sinistral strike-slip faulting along NE-SW striking faults such as the Akhurian and East Anatolian faults, (3) shortening along nearly E-W striking faults such as the Bitlis suture zone, and (4) normal faulting along ~N-S striking faults which form pull apart basin at the northern termination of the Zagros MRF (Fig. 1b).

The estimated macroseismic regions of the large historical and instrumental earthquakes (yellow ellipses in Fig. 1b) and the epicenters of instrumental earthquakes with  $M_w \geq 4$  (purple circles in Fig. 1b) mostly fall along the block boundary faults such as the Chalderan, Gailatu-Khoy, and North Tabriz fault systems (Ambraseys, 2009; Berberian, 2014; Selçuk et al., 2016). Occurrence of large earthquakes such as the 1930 Salmas earthquake and the Qotur doublet reveals that deformation in the study area is not completely concentrated along the block boundaries and could partially be accommodated along active faults within the blocks.

#### 3. Data and methods

#### 3.1. Earthquake location

We relocated the Qotur cluster using the *mloc* multiple-earthquake relocation technique specialized for calibrated (i.e., minimally biased hypocenters and quantifiable estimates of uncertainty) earthquake location studies to understand the relationship between seismicity and active faulting in the study area. The *mloc* method is based on the Hypocentroidal Decomposition (HD) algorithm (Jordan and Sverdrup, 1981) which we routinely utilized in many studies (e.g., Ghods et al., 2012, 2015; Zanjani et al., 2013; Nissen et al., 2019; Aflaki et al., 2019; Bergman et al., 2022). Recently, Karasözen et al. (2019) used *mloc* to provide a ~ 70-year catalog of instrumentally-recorded seismicity in the Zagros.

The events have been relocated using phase readings from permanent seismic stations of the Iranian Seismological Center (IRSC; htt p://irsc.ut.ac.ir/), Iranian National Seismograph Network (INSN; htt p://www.iiees.ac.ir), the Turkish AFAD and KOERI regional networks, the Incorporated Research Institutions for Seismology (IRIS) and the International Seismological Center (ISC; https://www.isc.ac.uk) (Fig. 2). The first author repicked all phase readings from permanent seismic stations in Iran. For some events, we have access to data from the Qotur BHRC (Building and Housing Research Center; https://ismn.bhrc.ac.ir/) accelerometer station with calibrated GPS timing. The station provided nearby readings for 24 events in the cluster including the first mainshock, which provided important constraint on event depth. All selected events have a Pg azimuthal gap of less than 150° but for most events the gap is less than 100°.

The Qotur cluster consists of 169 events that are part of the 2020 Qotur doublet between September 2019 and June 2020 plus two older events. The event magnitudes range from 1.9 to 6. We used only direct phases with epicentral distances  $D \leq 1.5^{\circ}$  to calculate the hypocentroid. The Turkish and Iranian seismic networks provided excellent Pg and Sg azimuthal coverage required to calibrate the absolute location of the cluster hypocentroid (Fig. 2).

We estimated the empirical reading error/uncertainty separately for each station-phase in the dataset to define and remove data outliers and to weight the data during the inversion procedure. For the subset of 24 events with nearby BHRC phase readings, we performed a trial-and-error search to estimate a best fitting Earth model with P and S velocities of 5.9 and 3.4 km s $^{-1}$  for the crustal layer and 8.3 and 4.7 km s $^{-1}$  for the mantle, respectively. The Moho is at 45 km depth. We relocated the subset while allowing *mloc* to calculate the focal depth of the hypocentroid and the events (i.e., free depth determination). After refining the velocity model, we relocated all events while fixing the depth of the event subset with nearby phase readings to those from the free depth

determination. We also tried to calculate focal depths for other less constrained events using nearby phase readings. The depth was estimated by minimizing the residual of nearby phase readings while giving more weight to the Pg phases. For events without nearby phase readings, we set the focal depth to that of the hypocentroid. A hypocentroid depth of 10 km is used for the cluster.

Direct calibration of a seismic cluster is possible if the lateral variation of the true velocity model relative to the averaged 1-D crustal model is insignificant. Previous studies indicate a strong gradient of P (Maheri-Peyrov et al., 2020) and S velocity (Mortezanejad et al., 2019) in the upper crust of the study area. P and S velocities are systematically larger to the east of the cluster. Since most Iranian stations east of the cluster are over ~100 km away, it is impossible to use only the arrival times at distances less than 50 km to avoid the velocity gradient and thus calibrate the cluster directly. Comparison of the InSAR modelled rupture plane with the epicenters of the direct-calibrated Qotur cluster shows a systematic ~4-km eastward shift. This is in agreement with the known faster and slower velocities to the east and west of the cluster, respectively. To overcome the eastward shift, we used the InSAR modeling results of the second mainshock as constraint to indirectly calibrate the cluster by shifting the whole cluster about 4 km normal to direction of the modelled InSAR rupture plane westward, so that the second mainshock lies on the trace of the modelled rupture plane. The relocation results are listed in Supplemental Table A1 and presented in the Results

#### 3.2. Focal mechanisms from waveform modeling

We performed regional moment tensor analysis for the two Qotur main events, two foreshocks, and 26 aftershocks. We used complete 3-component broadband waveforms for deviatoric moment tensor inversions applying the code of Nábělek and Xia (1995), which we have employed successfully in the past (e.g., Braunmiller and Ghods, 2021; Braunmiller and Wetmore, 2024).

The broadband data are from the Iranian IRSC and INSN networks, the KOERI network in Turkey, and from additional stations, mainly in the Caucasus region, archived at the IRIS DMC and Geofon data centers. We deconvolved instrument responses, rotated horizontal components to radial and transverse correcting, where necessary for documented sensor misorientations (Braunmiller et al., 2020; Büyükakpinar et al., 2021), and selected displacement seismograms for inversion based on visual inspection eliminating noisy traces. We used, on average, data from 27 stations and 52 components with a minimum count of 8 stations and 17 components for the 16:56 UTC aftershock on 23 February 2020. The data cover a distance range from about 100 km to 1000 km depending on signal strength and noise level.

Synthetics are calculated for a simple 1-D crustal model with a Moho depth of 46 km that we routinely use for moment tensor analysis in Iran. The 1-D modeling approach is adequate for our long-period analysis. Most events were analyzed at periods  $T \geq 18$  s with the long-period cutoff adjusted between T=30 s and 50 s based on event size and considering the medium bandwidth of some sensors. Centroid depth is found by grid-search with a 1-km step-size around the best-fitting depth. We estimated the range of acceptable solutions from the variance increase relative to the best-fitting solution. We used a 5 % variance increase as cut off for centroid depth and double couple source parameters (strike, dip, and rake) as waveform fits degrade visibly for larger variance increases.

For the mainshocks we show (in the appendix) waveform fits for selected stations and plots of variance as a function of centroid depth and double couple parameters, as well as results from a double couple grid search that more fully illustrates parameter trade-offs and uncertainties. The focal mechanisms, centroid depths and moment magnitudes of all 30 moment tensor solutions are listed in Supplemental Table A2.

#### 3.3. Fault geometry and slip distribution from InSAR

We estimated the areal extent of the surface deformation related to the 2020 Qotur earthquake doublet using three sets of C-band (wavelength of 5.6 cm) imagery from the European Space Agency Sentinel 1 A and 1B satellites. We used the NSBAS software to generate interferograms (Marie-Pierre Doin et al., 2011) from SLC (Single Look Complex) products. A DEM from the Shuttle Radar Topography Mission (SRTM) with 90 m resolution was employed to correct for the topographic phase (Farr and Kobrick, 2000). In our processing using the NSBAS package, the ERA5 atmospheric reanalysis data provided by ECMWF (Hersbach et al., 2020) are interpolated both vertically and horizontally to match the geometry of each interferogram. Vertical interpolation is carried out on the pressure levels provided by ERA5 (typically 37 standard levels from 1000 hPa to 1 hPa) using linear interpolation in pressure coordinates to estimate the atmospheric delay along the radar line-ofsight. Horizontal interpolation is performed via bilinear interpolation from the native ERA5 grid (0.25 $^{\circ}$   $\times$  0.25 $^{\circ}$  resolution) to the SAR image grid. These interpolation steps are implemented within the default NSBAS atmospheric correction module (Doin et al., 2009; Jolivet et al., 2011). No spline interpolation or tension parameters are applied. All available ERA5 vertical levels were used in our processing. Finally, the delay map corresponding to the interferogram was calculated by subtracting the tropospheric corrected delay maps at the time of the two acquisitions (Jolivet et al., 2011). The resulting interferograms were smoothed with the Goldstein filter (Goldstein and Werner, 1998). Then, phase unwrapping has been applied with the branch-cut method (Gutmann and Weber, 1999).

To validate the effectiveness of the tropospheric correction using ERA5 data, we calculated the RMS misfit between the observed and modelled interferograms before and after applying the correction. Since our study area is mountainous and thus particularly susceptible to stratified atmospheric delays, the correction had a notable impact. For the ascending track, the RMS decreased from 5.6 cm to 3.6 cm, representing a  $\sim 36~\%$  reduction. For the descending track, the RMS decreased from 5.8 cm to 4.3 cm, corresponding to a  $\sim 26~\%$  reduction. These improvements demonstrate the effectiveness of the ERA5-based correction in mitigating atmospheric noise and enhancing the quality of the coseismic signal.

Table 1 shows details of the processed images used to create the coseismic interferograms. Fig. 2 shows the area covered by the interferograms. We processed the shortest available spatial and temporal baseline of the S1-TOPS C-band SAR imagery to improve the interferogram coherency and avoid any early postseismic displacement, respectively. We processed an ascending (A72) track with 32 m and 12 days of perpendicular and temporal baselines to obtain the surface deformation of the first mainshock. The second mainshock was covered by one ascending (A72) and one descending (D152) track with 12 and 6 days of temporal baseline, respectively. Acquisition of the S1 ascending and descending SAR imagery about one and 9 h before the the second mainshock (16:00 on 23 February 2020), respectively, allowed us to retrieve the coseismic displacement for each main earthquake

**Table 1**Interferograms constructed for the Qotur doublet. EQ1 and EQ2 are the first and second event of the doublet, which occurred at 5:52 UTC and 16:00 UTC on 23 February 2020, respectively.

	Orbit	Path	Master-Slave	Perpendicular Baseline (m)	Δt (day)
EQ1	Ascending	72	2020.02.17 (15:01) -2020.02.23 (15:00)	32	12
EQ2	Ascending	72	2020.02.23 (15:00) - 2020.03.06 (15:01)	3	12
242	Descending	152	2020.02.23 (07:31) -2020.02.29 (03:09)	124	6

separately.

The ascending and descending displacement maps of the second mainshock are used to jointly invert for the causative fault plane parameters. We applied a coherence threshold of >0.2 when selecting interferogram pixels for further processing. This relatively low threshold was chosen to retain more signals in decorrelated regions while still excluding noise-dominated pixels. We found that the threshold provides a good balance between preserving spatial coverage and maintaining data quality, particularly in areas affected by moderate temporal decorrelation. To obtain the source parameters, the selected pixels of the unwrapped LOS surface displacements were first down-sampled using a quadtree algorithm (Jónsson et al., 2002) and then inverted to infer the geometry of a single rectangular plane with uniform slip in a uniform elastic half-space (Okada, 1985). We considered the stopping criterion for the quadtree down-sampling as variance threshold of 6 mm<sup>2</sup> and 3 mm<sup>2</sup> for ascending and descending, respectively. The criterion resulted in approximately 719 and 1030 quadtree nodes, respectively.

The fault geometry parameters are location (X, Y, and depth), size (length and width), orientation (strike, dip, and rake), and uniform slip of the rupture plane. We assume the X, Y, and depth to correspond to the center of the top edge of the rupture plane. We obtained the source parameters by minimizing the squared misfit between the observed and modelled displacement in the inversion procedure (Minson et al., 2013) using a nonlinear inversion method as implemented in the open-source Geodetic Bayesian Inversion Software (GBIS) released by Centre for Observation and Modeling of Earthquakes, Volcanoes, and Tectonics (COMET) (Bagnardi and Hooper, 2018). The inversion code uses a Markov-chain Monte Carlo algorithm (Hastings, 1970) incorporating the Metropolis-Hastings algorithm to estimate the multi-variate posterior probability distribution for all model parameters. We used Okada's (1985) displacement Green's functions and assumed a shear modulus of 30 GPa and a Poisson ratio of 0.25 to model the displacement field. Uniform priors were used for location and geometry parameters such as strike, dip, and rake (Table S1).

Once the geometry of the fault plane with a uniform slip was estimated, we expanded the rupture plane 20 km along-strike and 12 km along the down-dip directions and divided it into 1291 individual triangular patches to obtain the slip distribution on the rupture plane. Each patch has a fixed geometry (i.e., fixed strike, dip and rake) according to the optimal source parameters obtained from the nonlinear modeling, and the slip was allowed to vary freely on the fault plane. The regularized linear inversion was then performed to estimate the variation of slip by minimizing  $\varphi$ ,

$$\varphi = \|G s - d\|^2 + \alpha^2 \|H s\| \tag{1}$$

where G are the dislocation Green's functions, s is variable slip on each patch of the rupture plane, d is the observed ground displacement from InSAR for each pixel, H is the finite difference approximation of the Laplacian operator and  $\alpha$  is a smoothing factor controlling the trade-off between data misfit and model roughness. The regularized least-squares optimization problem (Eq. 1) is solved using a smoothing factor of  $\alpha=0.52$  as determined by an L curve plot (Fig. S1). We used a modified version of the open-source software FaultResampler 1.4 to perform the linear inversion for calculating slip distribution on the rupture plane (Barnhart and Lohman, 2010).

#### 3.4. Estimation of the state of stress

We deduced the stress regime in the study area using the focal mechanisms of the thirty 2020 Qotur events and the 1930 Salmas 7.1  $M_{\rm w}$  earthquake listed in Table A2. We applied the FCALC – Geodyn-Soft software (Carey-Gailhardis and Mercier, 1987) to perform the stress tensor inversion (Carey-Gailhardis and Mercier, 1987; Shabanian et al., 2010). The resulting stress states are well-constrained tensor solutions defined by two main criteria. First, the obtained stress ratio [R = ( $\sigma_2$  –

 $\sigma_1)/(\sigma_3-\sigma_1)]$  should be compatible with the observed fault kinematics, and the resulting Andersonian stress axes. Second, on each fault plane, the misfit angle between the rake of the slip vector obtained from the focal mechanism solution and the calculated one should be less than  $25\text{--}30^\circ.$ 

#### 4. Results

#### 4.1. The first mainshock

Our *mloc* relocation includes five foreshocks with magnitude between  $M_L$  2.7 and 4.2 that started about one week before the first mainshock occurred. Combined with three additional events that happened between February 2009 to November 2019 (magnitudes from  $m_b$  3.6 to 4.8), these eight earthquakes perhaps already show activity on a conjugate fault set (Fig. 3a) outlining the initial conjugate elongated aftershock cloud pattern (Fig. 3). The focal depth of the first mainshock is well constrained at 10 km depth using the nearby phase readings (epicentral distance of  $\sim$ 9 km) from the Qotur BHRC accelerometer station and is consistent with the centroid depth of 9 km from regional waveform modeling (Table A2). Our moment magnitude of 5.73  $M_w$  is slightly less than the 5.8  $M_w$  reported by the Global CMT project. The focal mechanism of the first mainshock is oblique strike-slip with a large normal component.

Fig. 4 shows the wrapped (a) and unwrapped (b) coseismic displacement of the first mainshock in the Line of Sight (LoS) direction in the ascending geometry, respectively. The maximum LoS displacement is ~4 cm and the interferogram pattern does not show any sign of surface rupture. The epicenter is close to the southeastern edge of the area with the largest LoS values. The lack of a clear interferogram pattern, though, precludes us from obtaining an independent estimate of the fault azimuth or type of faulting for the first mainshock. Simple forward models of the first mainshock display very low amplitude surface displacements similar to those observed regardless of the fault strike. We simulated LOS displacements assuming a constant slip of ~30 cm on a 5  $\times$  5 km fault plane at 9 km centroid depth, consistent with the estimated parameters of the first mainshock (5.9 Mw), for both NE- and NWtrending fault planes. To allow for a meaningful comparison, we generated the synthetic interferograms for the ascending track. The resulting surface displacements are below ~2 cm in both cases (Fig. S2). The low amplitude is comparable to the background noise level in the actual interferograms. The results support the conclusion that such small coseismic signals are below the detection threshold of InSAR in this region. For both fault orientations using a shallower centroid depth of 5 km would result in more than 4 cm surface displacement which is larger than observed for the first mainshock (Fig. S3). The models further confirm that the first mainshock was deeper than the second mainshock. Figs. 3b and 4b show that aftershocks after the first and before the second mainshock are mainly elongated in a NE-SW direction suggesting rupture during the first mainshock might have occurred along a NE-SW trending fault.

Most aftershocks are located NE of the epicenter of the first mainshock implying that the rupture propagated mainly towards NE. The Makhin, Habash Sofla and Zeri villages north of the epicenter suffered some partial damage due to the first mainshock (Taymaz et al., 2022), therefore, the spatial distribution of the damaged villages is in agreement with a NE directivity of the first mainshock. The small LoS amplitude precludes modeling the fault geometry of the first mainshock, but is in agreement with the larger focal depth of 10 km (Table A1) and centroid depth of 9 km (Table A2), and lack of serious effects on residential areas.

#### 4.2. The second mainshock

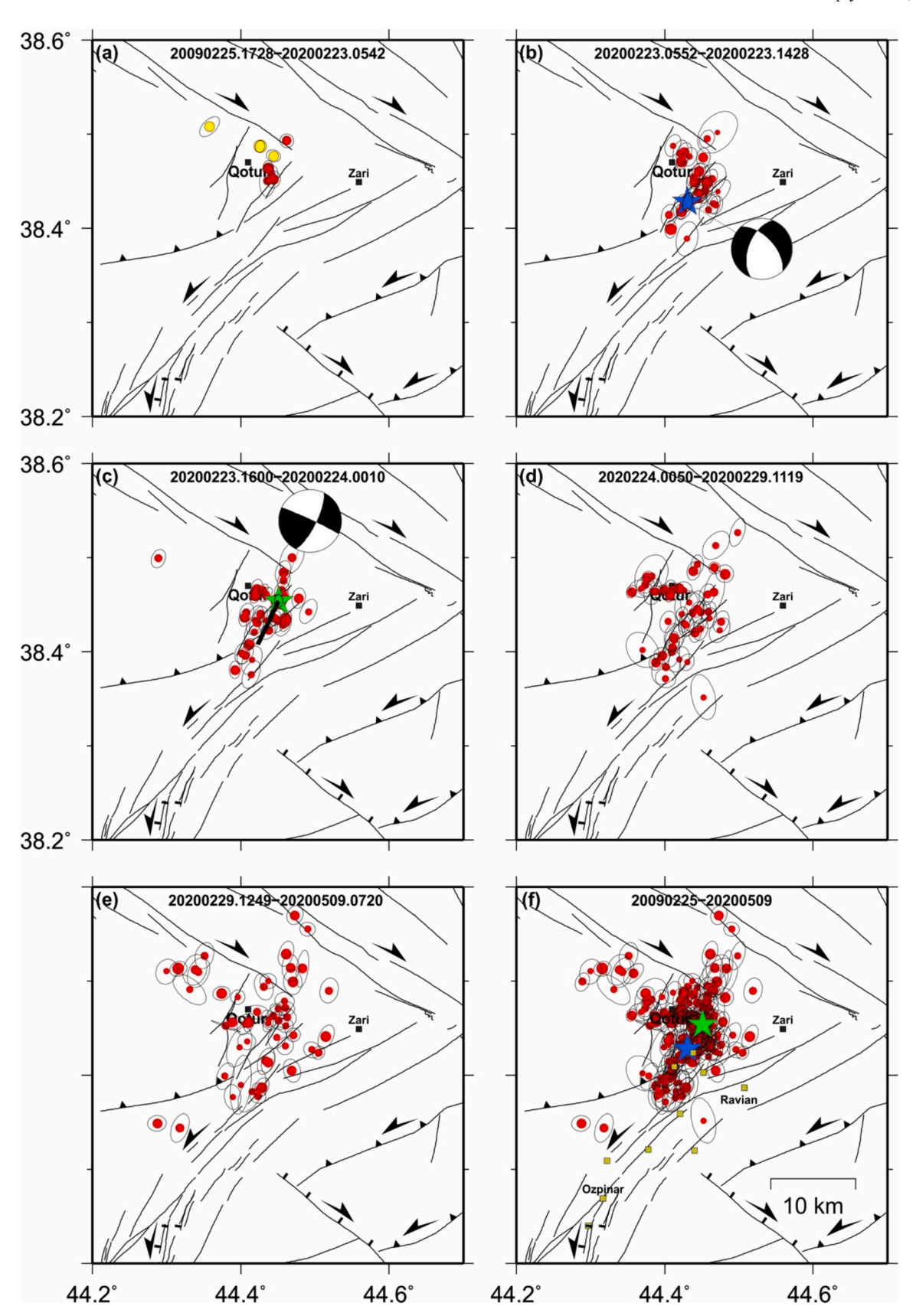
The epicenter of the second mainshock is about 3 km NE of the epicenter of the first mainshock (Fig. 3f). Our moment tensor solution

indicates a magnitude of 5.9  $M_w$  that is slightly smaller than 6.0  $M_w$  reported by the Global CMT Project, which is mainly due to centroid depth differences. The moment tensor shows an almost perfect strikeslip mechanism. Fig. 3c shows that the first 30 aftershocks, which occurred within 8 h of the second mainshock, form an elongated  $\sim\!15~km$  long NE-SW trending aftershock cloud. The cloud extends mainly towards the southwest of the epicenter of the second mainshock suggesting mostly unidirectional SW-directed rupture. Its focal depth, though, is not well-constrained because of a lack of readings from nearby seismic stations. Our centroid depth for the second mainshock of 5 km is shallower than the 9-km centroid depth of the first mainshock.

Fig. 5 shows the coseismic deformation field of the second mainshock. The ascending and descending Sentinel-S1 image (A72) (Fig. 2) were acquired about one and 8.5 h before the second mainshock (Table 1). This fortunate coincidence ensures that the corresponding coseismic interferograms exclude the coseismic displacement of the first mainshock. The butterfly shapes of the fringes in the coseismic displacement maps in both ascending and descending geometries demonstrate clearly that the earthquake involved a significant strike-slip motion. The pattern of the fringes shows no sign of surface rupture. The unwrapped coseismic interferograms (Figs. 5c and d) reveal a maximum of 25 and 15 cm displacement in the LoS direction for the ascending and descending images, respectively. The LoS displacement of the second mainshock (Figs. 5a and b) is much larger than that of the first mainshock (Fig. 4) in agreement with its inferred shallower depth and larger magnitude. The deformation patterns in the ascending and descending interferograms differ because of varying LoS relative to the fault motion. Comparing the wrapped interferograms in the ascending (Fig. 5a) and descending (Fig. 5b) geometries shows that the displacement in the left lobe of the ascending track is larger than in the descending one. Considering the satellite motion direction, this implies that the rupture plane and the satellite were getting closer to each other. This projection of ground motion on the two different LoS is the reason for the difference between the maximum displacement of the ascending and descending interferograms. Considering the focal mechanism of the second mainshock, the distribution of its aftershocks (Fig. 3d), and its coseismic displacement (Fig. 5c and d), the NE-SW left-lateral strike-slip fault is considered to be the rupture plane. Figs. 5e and f show the vertical and horizontal components decomposed from the ascending and descending LoS displacement maps. The displacement in the vertical direction (Fig. 5f) is much smaller than in the horizontal direction (Fig. 5e) consistent with the almost pure strike-slip focal mechanism of the second mainshock.

The simultaneous inversion of the ascending and descending displacements to obtain the uniform slip solution has been performed with the parameters listed in Table 2. The lower and upper parameter bounds, which describe the fault plane geometry, are based on constraints from the seismicity pattern (Fig. 3) and visual interpretation of the interferograms (Fig. 5). Table 2 shows the resulting best-fit rupture plane geometry from Bayesian inversion and compares it with the rupture parameters from our moment tensor solution. The observed and modelled wrapped displacement fields, and the corresponding residual interferograms are shown in Fig. 6. Fig. A5 presents the a-posteriori probability distribution showing the trade-offs between the estimated fault parameters. The scatter plots indicate that all parameters were well-resolved within the a priori bounds given in Table 2. The model parameters for a constant slip model (Table 2) correspond to a northeaststriking (N24°) left-lateral rupture plane dipping  $\sim$ 86° towards the east. The constant slip model did not fully reproduce all observed fringes (Fig. 6 and A6) and has a maximum displacement residual of ~9.1 and 6.5 cm in the ascending and descending displacement fields (Figs. 6c and f), respectively, which could be due to variable slip on the rupture plane.

Using the geometrical constraints from the constant slip modeling (Table 2), we next inverted for distributed slip on the rupture plane. Fig. 7 shows the observed (a, d), modelled (b, e), and residual (c, f) displacements in the ascending and descending geometries,



(caption on next page)

Fig. 3. The 169 Qotur relocated events are shown with active fault traces in the background for five periods (a-e) and the entire period (f) to illustrate the evolution of the sequence. a) 2009/02/25–2020/02/23. The eight events that occurred before the first mainshock perhaps suggest activity on a conjugate fault system. Three pre-2020 events are shown as yellow circles, b) First mainshock to 14:28 UTC 2020/02/23. Locations of the first mainshock (blue star) and its first 12 aftershocks are consistent with rupture on the NE-SW trending nodal plane, c) 16:00 UTC 2020/02/23 to 00:102020/02/24. Second mainshock (green star) and immediate aftershocks. The locations, combined with the surface trace of the preferred causative fault of the second mainshock from InSAR modeling (shown as a thick grey line), suggest unilateral southwest-directed rupture, d) 00:50 UTC 2020/02/24 to 11:192020/02/29, and e) 12:49 UTC 2023/02/29 to 07:20 UTC 2020/05/09. d) and e) show spreading of the aftershock zone and increased involvement of the northwest-trending conjugate fault system. f) All 169 relocated events in the Qotur seismic cluster from 2009/02/25 to 2020/05/09. The first and second mainshocks are shown as blue and green stars, respectively. Villages where most damage occurred are shown with yellow rectangles (Taymaz et al. (2022) and references therein). All villages are southwest of the main events supporting our argument that the second event propagated unilaterally towards the southwest. The focal mechanisms of the first and second events (in b) and c)) are from this study. Relocations are listed in Supplemental Table A1. (For interpretation of the references to colour in this figure legend, the reader is referred to the web version of this article.)

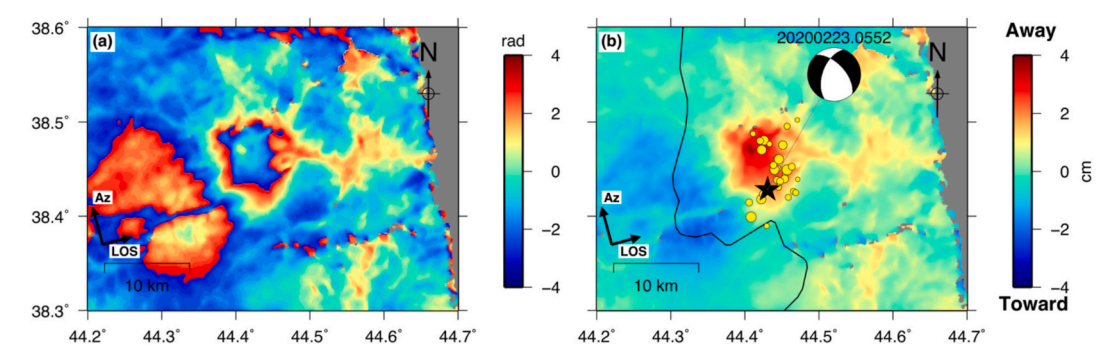


Fig. 4. Wrapped (a) and unwrapped (b) coseismic displacement field in the LoS direction from Sentinel-1 data in the ascending orbit for the first mainshock. Positive (red) and negative (blue) values in the unwrapped interferogram indicate displacement away from and towards the satellite, respectively. The first mainshock is marked by a black star; yellow circles are aftershocks for period between the two main events, namely from 20,200,223.0600 to 20,200,223.1428. (For interpretation of the references to colour in this figure legend, the reader is referred to the web version of this article.)

respectively. Figs. 7g and h show the fault-slip distribution and its standard deviation, respectively. Fig. S4 demonstrates that the distributed slip models yield significantly smaller RMS misfits than the uniform slip models for both ascending and descending tracks. The RMS misfits for the uniform slip models are 9.1 cm (ascending) and 6.5 cm (descending), whereas the distributed slip models produce much better fits, with RMS values of 3.3 cm (ascending) and 2.1 cm (descending).

The slip distribution (Fig. 7g) shows that the coseismic rupture is concentrated around 3 km depth where we obtained maximum slip estimates of  $97\pm8$  cm, where the  $\pm8$  cm uncertainty reflects the standard deviation of the slip distribution. The top of the area with large slip reaches upward to a depth of 1.4 km but did not reach the surface consistent with the lack of observed surface ruptures and the InSAR fringe pattern. According to our slip model, the mainshock occurred on a NE-SW striking fault plane dipping towards the east. Assuming a rigidity of 30 GPa, the geodetic moment is 1.52E+18 Nm, equivalent to a moment magnitude of 6.05 Mw. The moment release is approximately 30 %, and 65 % larger than moment estimated seismically from the Global CMT and our moment tensor analysis, respectively. Part of the discrepancy might be due to some postseismic slip included in the InSAR modeling.

#### 4.3. The temporal evolution of the aftershock cloud

Fig. 3 shows the space-time evolution of the Qotur aftershocks. The space-time evolution suggests that the cluster involved at least two conjugate perhaps crossing, right and left-lateral strike-slip faults. The Qotur mainshocks ruptured along NE-SW trending faults parallel to and aligned with the NE-elongated aftershock cloud. The second, larger mainshock occurred about 3 km NE of the first mainshock. The aftershock cloud after the second mainshock forms a clear NE-SW trend (Fig. 3c) suggesting a SW directivity for the rupture of the second mainshock. The rupture directivity is further supported by the spatial distribution of the damaged villages (Fig. 3f) which are concentrated SW of the epicenter of the second mainshock. With time, the aftershock cloud grows and includes activity on a conjugate NW-SE trending

lineament. We suggest that initially the seismicity is following a NE-SW trend aligned with the Bashkale fault system. But later seismicity also occurs on NW-SE trending right-lateral strike-slip faults conformant with the trend of the Salmas fault. The left-lateral NE-trending and the right-lateral NW-trending strike-slip fault systems intersect near the epicenter of the second mainshock but shallow aftershock activity, predominantly with oblique normal faulting mechanism (Fig. 8) extends for about 10 km further to the north and also five km to the south of the southern end of the NW-trending modelled fault (Fig. 3f).

## 4.4. The distribution of focal and centroid depths

We could determine reliable focal depths for 24 events including the first mainshock using the nearby Qotur BHRC accelerometer station (Fig. 8a). The focal depths are distributed between 3 and 14 km (Fig. 7g). The centroid depths of the 30 moment tensor solutions are between 3 and 14 km (Fig. 8b) except for a single outlier at 20 km depth (and large uncertainties). We note that the focal and centroid depths are mostly deeper than the main slip patch of the rupture plane inferred from InSAR modeling (Fig. 7g) of the second mainshock.

#### 4.5. Active tectonics and the state of stress

We estimated the stress regime using the 30 focal mechanisms of the foreshocks, mainshocks, and aftershocks of the 2020 Qotur doublet (Table A2) together with the focal mechanism of the 1930 Salmas 7.1 M<sub>w</sub> earthquake (Jackson and McKenzie, 1988). The focal mechanisms are either strike-slip or normal with a strike-slip component, therefore, the data were separated into strike-slip and extensional clusters. For each event, we used the nodal plane that we think represents the likely fault plane. Based on the shape of relocated aftershock cloud and our InSAR modeling, for those events lying on the main NE-SW trending branch of the aftershock cloud we selected the NE-SW striking nodal planes as the causative fault plane. For those events lying along the NW-SE trending branch of aftershocks, we selected the NW-SE striking nodal planes as the causative fault plane. For the 1930 Salmas

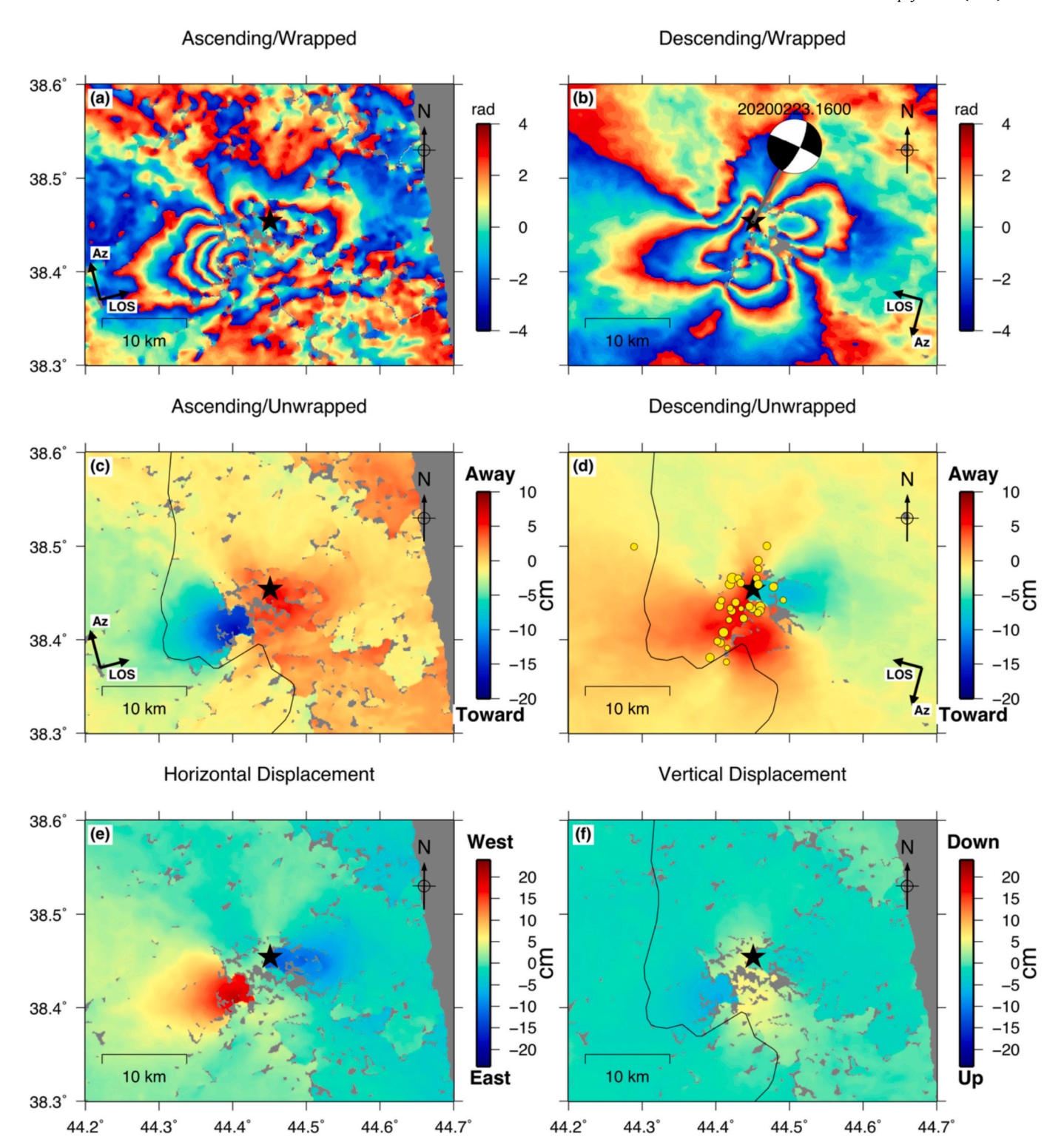


Fig. 5. LoS coseismic deformation fields for the second mainshock. Wrapped and unwrapped interferograms are generated from Sentinel-1 data pairs acquired along ascending (a, c) and descending (b, d) orbits, respectively. The corresponding horizontal and vertical displacements are shown in (e) and (f), respectively. The second mainshock is marked by a black star. The yellow circles (in d) show aftershocks as in Fig. 3c. (For interpretation of the references to colour in this figure legend, the reader is referred to the web version of this article.)

earthquake, the reported NW-SE striking nodal plane is compatible with the earthquake surface rupture (Berberian and Tchalenko, 1976) and is selected as the fault plane.

The nodal planes of the strike-slip focal mechanisms reveal either dextral or sinistral slip along the NW-SE and NE-SW striking fault planes, respectively. The normal focal mechanisms present normal-to-oblique-

sinistral slip along nearly N-striking fault planes and normal-to-dextral slip along NW-SE striking faults. The stress inversion result for the strike-slip cluster shows a transtensional stress regime with an NNW-SSE direction of the horizontal  $\sigma_1$  stress axis. The normal faulting data reveal an extensional stress regime with an ENE-WSW direction of the horizontal  $\sigma_3$  stress axis (Fig. 9). The directions of the maximum and

Table 2
Fault parameters of the best-fit uniform slip solution of the second mainshock along with the range of lower and upper bounds for different parameters. For comparison, we show the fault parameters of the second mainshock from moment tensor analysis (Table A2). Depth for InSAR means center of the top edge of the rupture plane and for the Moment tensor is centroid depth.

Parameter	Lon (°)	Lat (°)	Length (km)	Width (km)	Depth (km)	Strike (°)	Dip (°)	Dip-slip (m)	Strike-slip (m)	Rake (°)	$M_{\rm w}$
Lower bound	44.39	38.375	4.5	3.0	1.0	10.0	65	-0.10	0.00	-	_
Upper bound	44.46	38.470	12.0	15.0	5.0	45.0	90	0.50	3.00	_	_
0 11 1	44.45	38.453	5.3	7.2	1.5	24.4	86	0.07	1.11		6.00
Optimal	$\pm 0.001$	$\pm 0.001$	$\pm 0.3$	$\pm 0.4$	$\pm 0.4$	$\pm 3$	$\pm 3$	$\pm 0.02$	$\pm 0.1$	4	6.22
Moment tensor	_	_	_	_	5.0	26	74			5	5.91

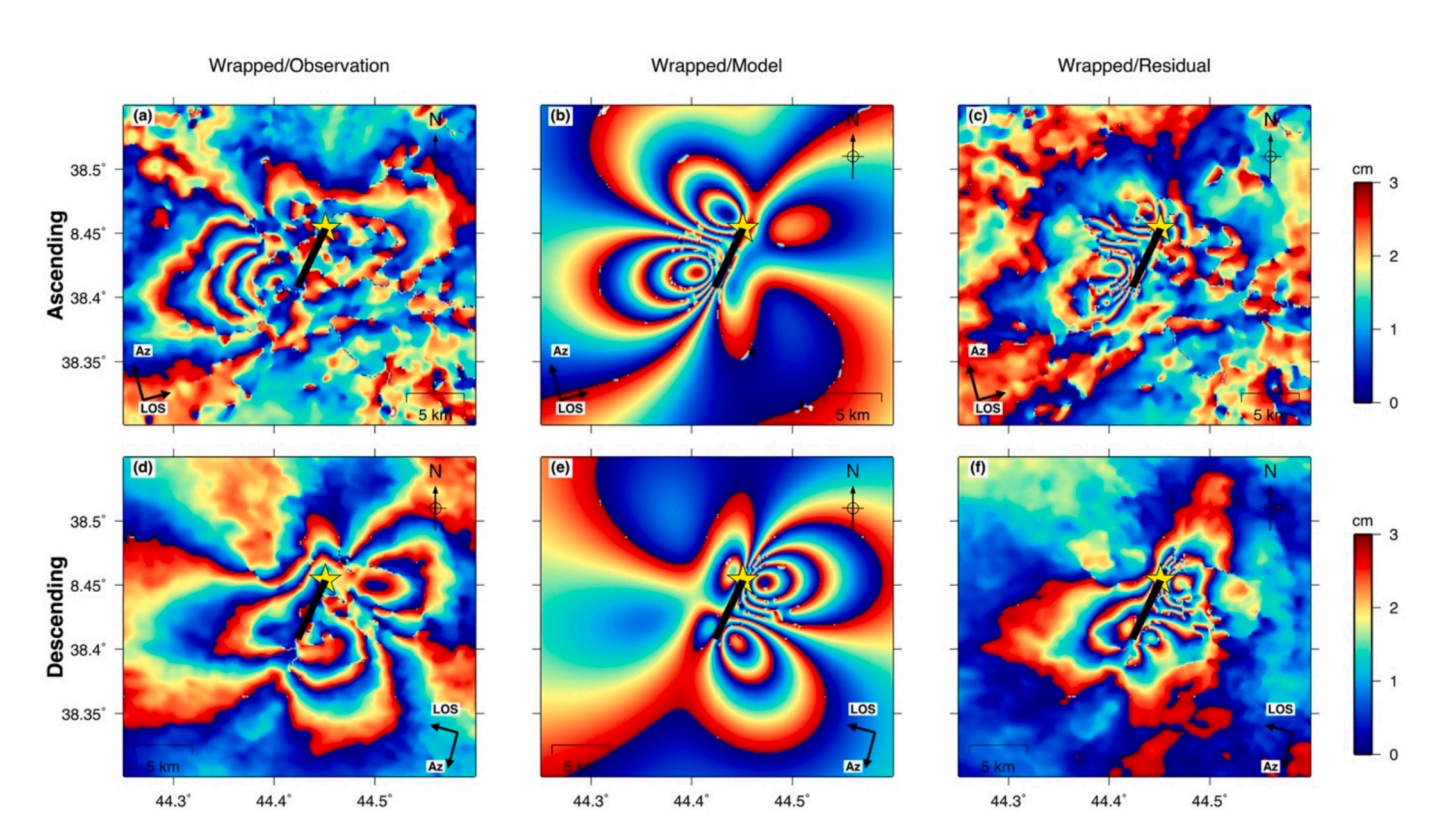


Fig. 6. (a, d) show Sentinel-1 observations (as in Fig. 5) and (b, e) and (c, f) model results and residuals from the uniform slip dislocation model for the second mainshock, respectively. The yellow star shows the epicenter of the second mainshock which lies at the northeast end of the modelled fault (the thick black line). (For interpretation of the references to colour in this figure legend, the reader is referred to the web version of this article.)

minimum horizontal stress axes are the same for both clusters underscoring that both are responding to the same tectonic regime.

The estimated stress regime agrees closely with the stress regimes inferred from the inversion of geologically measured fault planes (Niassarifard et al., 2021) in the southern part of our study area. They present a regional stress regime with a NE-SW direction of the  $\sigma_1$  stress axis together with a local strike-slip regime with an NNW-SSE direction of the  $\sigma_1$  stress axis in the western part of Urmia Lake. The measured normal fault planes in the Serow pull-apart basin, SE of the Bashkale depression, present local horizontal extension in an ENE-WSW direction. The obtained stress field is also compatible with the area's morphotectonic features. The Qotur earthquakes occurred at the northern termination of the Bashkale depression. The morphotectonic features within the Bashkale depression deduced from satellite images show sinistral displacement along  $\sim$ NE-SW trending faults and normal scarps along  $\sim$ NNE-SSW to N-S trending faults.

#### 5. Discussion

Through careful earthquake relocation of the seismic cluster, we have shown that the Qotur doublet ruptured along NE-SW trending left-

lateral strike-slip faults in agreement with the trend of faults in the northern part of the Bashkale fault system. We have also shown that the aftershock cloud spreads over time and involves additional conjugate NW-SE trending right-lateral strike-slip faults oriented as the Salmas fault. Our results suggest that the crossing right- and left-lateral strike-slip faults of Bashkale-Serow fault system are concurrently seismically active.

Our relocation results are different from those of Taymaz et al. (2022) who did not find a clear relationship between their relocated earthquake cloud and the two possible fault planes suggested by their fault plane solutions. We suspect the main reason for the difference is that Taymaz et al. (2022) included events with large Pg azimuthal gaps. Similar to our approach, the authors first merged Iranian and Turkish seismic data but kept a considerable number of aftershocks with large Pg azimuthal gaps in their 500-event dataset, which led to a scattered earthquake cloud. We, instead, included only events with Pg azimuthal gaps of less than 150° and, using our multiple event relocation method, reduced location biases introduced by the earth model and bad phase readings.

Taymaz et al. (2022) suggested that the Qotur doublet ruptured two separate NW-SE trending fault planes. From the two planes obtained by

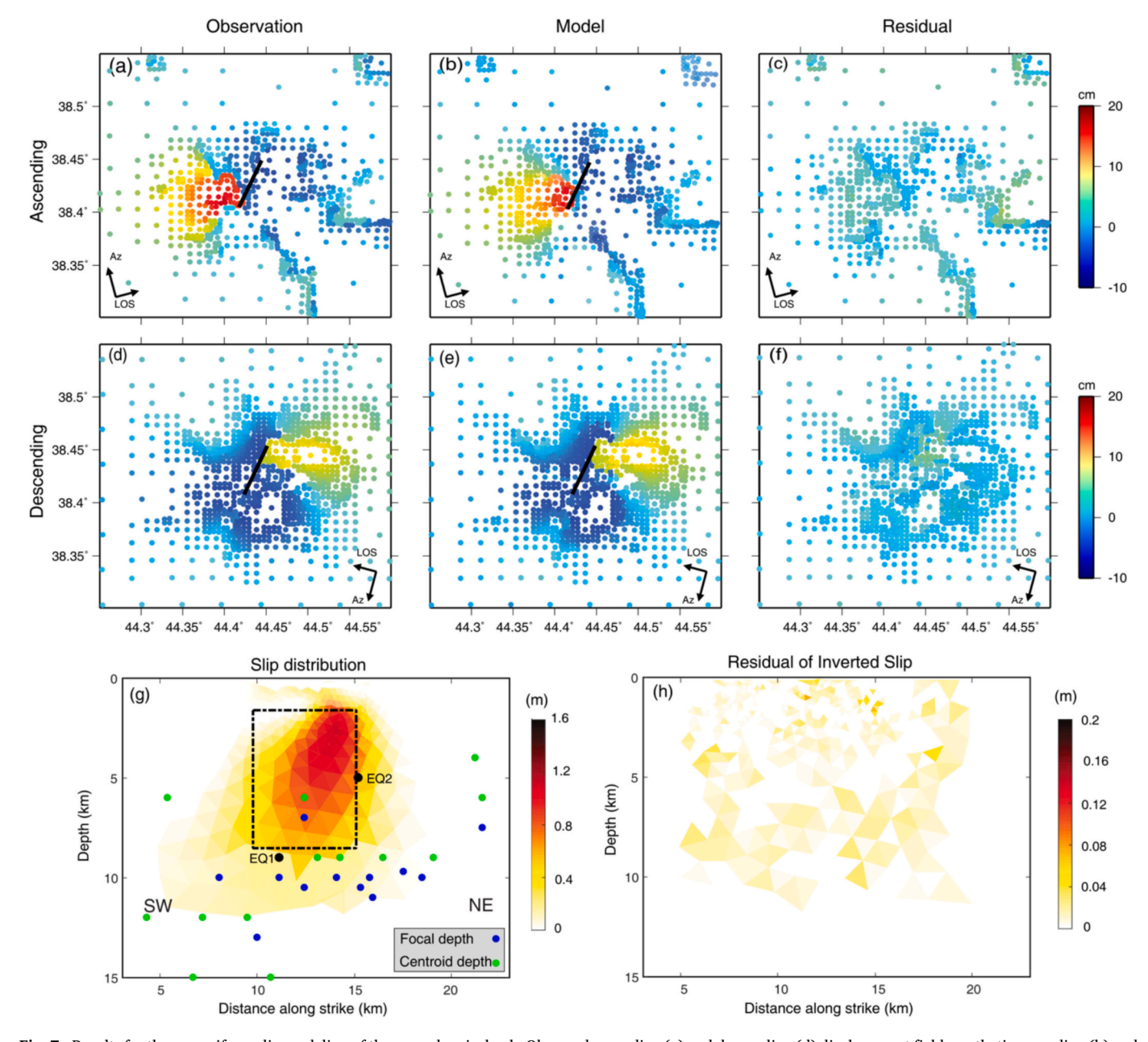


Fig. 7. Results for the nonuniform slip modeling of the second mainshock. Observed ascending (a) and descending (d) displacement field, synthetic ascending (b) and descending (e) displacement fields, and ascending (c) and descending (f) residual displacement fields. Black lines show the location of the fault plane when projected to the surface. g) Best-fitting distributed slip resulting from the least-squares inversion of InSAR data; the black dashed rectangle shows the slip region of the uniform fault slip model (Table 2); mainshock centroid depths are marked by black circles (EQ1 and EQ2) and aftershocks with reliable focal or centroid depths are shown as blue and green circles, respectively, h) Standard deviation of the distributed slip. The slip distribution from nonuniform (g) and uniform (Table 1) slip modeling suggest the fault rupture did not reach the surface consistent with field observations (Esmaeili et al., 2020). (For interpretation of the references to colour in this figure legend, the reader is referred to the web version of this article.)

their point source focal mechanism, they selected the NW-SE trending planes and estimated the slip distribution on these planes by jointly inverting teleseismic and local seismic data for a finite fault model. They assumed that the relocated earthquake distribution and InSAR interferograms images are consistent with NW-SE trending fault planes. Their finite fault modeling predicts some minor surface rupture for the first mainshock and significant surface rupture (20–40 cm over a  $\sim 3–5$  km length) for the second mainshock in contrast to the lack of any observed surface rupture. Taymaz et al. (2022) suggested that the lack of observed surface ruptures in the InSAR data may be related to a thick snow cover, however, the penetration depth of the C-band SAR imagery is about 9 m (e.g., Rignot et al., 2001), which far exceeds the maximum

reported snow cover of 1.5 m (Taymaz et al., 2022) at the time the events occurred. Taymaz et al. (2022) mainly used the interferograms to infer the strike of the causative faults for the Qotur doublet. InSAR interferogram images can discern the rupture plane from its auxiliary plane for strike slip events if there is a surface rupture. Due to lack of surface rupture, we used the pattern of precisely relocated earthquakes (Fig. 3), the location and direction of the reported NE-SW trending surface fractures (Esmaeili et al., 2020), and the spatial distribution of damaged villages (Fig. 3) to infer NE-SW trending fault as the causative fault for the second mainshock. Unlike Taymaz et al. (2022), we used ascending and descending InSAR images jointly to model the rupture plane. This is important because the ascending InSAR image (Fig. 6a) is

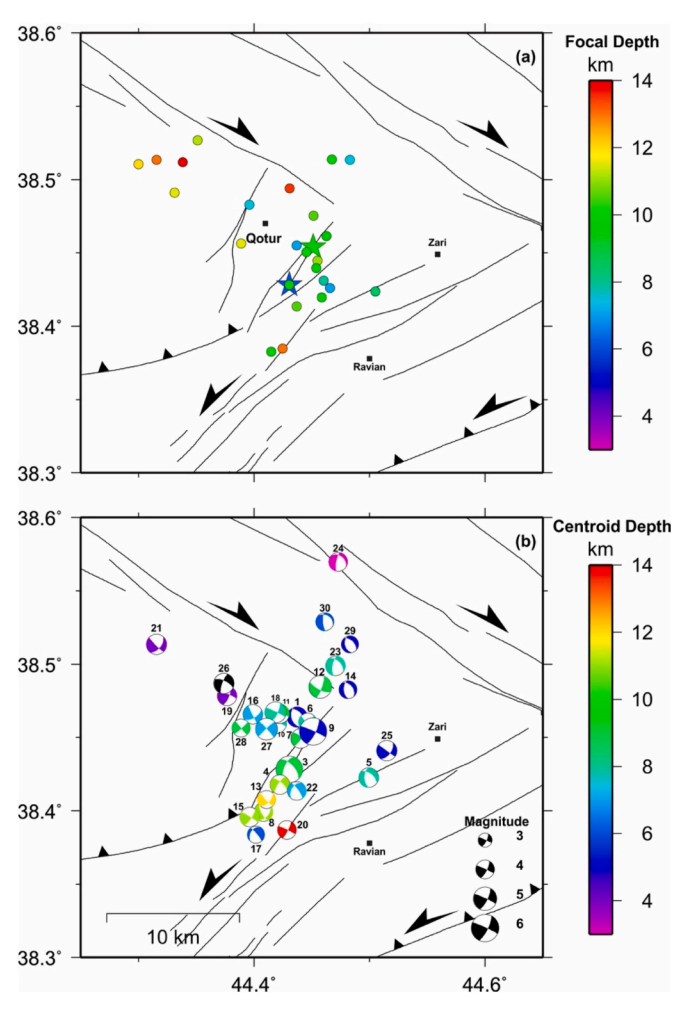


Fig. 8. a) Depth of 24 earthquakes with precise focal depth determination from phase readings at the nearby Qotur BHRC accelerometer (labeled 'n' in column 'D' of Table 1). b) Focal mechanisms of the event doublet (#3 and #9) and 28 fore- and aftershocks from moment tensor inversion plotted at their *mloc* relocations. Colour indicates centroid depth. The depth range is 3–14 km as for the focal depths in a), except for event #26 with a centroid depth of 20 km (with bounds of -8/+7 km from variance increase, see Section 3.2). Numbers above the focal mechanisms are keyed to the moment tensor solutions in Table A2.

very noisy and thus calculating displacement field along rupture plane using only the ascending image would be unreliable.

Two other studies derived faulting models for the Qotur sequence based on relocating aftershocks combining phase data from Iranian and Turkish seismic networks reaching contradicting conclusions. Taymaz et al. (2022) favor rupture on NW-SE trending faults and Rezapour (2024) on NE-SW trending faults (similar to us). Both groups applied HypoDD (Waldhauser and Ellsworth, 2000) to relocate events with 'good azimuthal' coverage using absolute travel-time picks from seismic stations at least 50 km from the epicentral region. Their results show broad distributions that could be interpreted in either way (NW-SE or NE-SW trending faults). Our stricter selection criteria for azimuthal gap combined with our analysis of the temporal aftershock evolution shows a NE-SW lineation of immediate aftershocks that resolves NE-trending fault planes confirmed by InSAR analysis, damage distribution, and distribution of surficial cracks. Given the large distances (D  $\geq$  50 km) and use of catalog travel times, we are suspicious about aftershock crosssections in Taymaz et al. (2022) and Rezapour (2024) as they likely lack sufficient depth resolution beyond the assertion that all aftershocks occurred in the upper 15-20 km of the crust (Fig. 8).

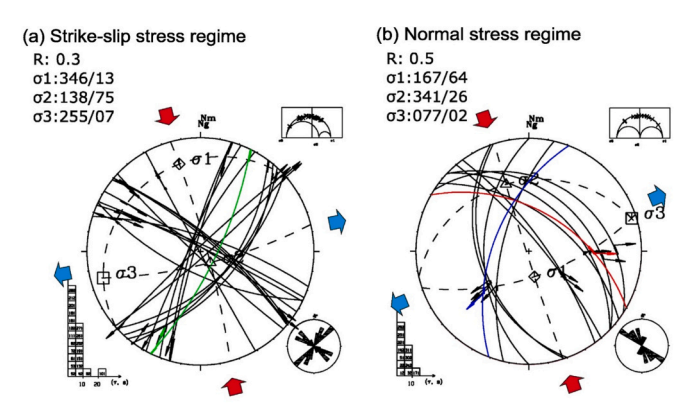


Fig. 9. Lower hemisphere stereographic projections of the strike-slip (a) and normal (b) stress regimes obtained from the fault plane solutions (Table A2) of the 30 Qotur events (see Fig. 8 for locations) and the 1930 Salmas earthquake. The stress ratio (R), the trend and plunge of the principal stress axes (upper left), the corresponding Mohr circle (upper right), misfit angles (lower left), and rose diagrams for strikes of fault planes (lower right) are also presented. Ng and Nm indicate direction of geographical and magnetic north. Blue, green, and red planes are the inferred causative faults of the first and second Qotur mainshock and the 1930 Salmas earthquake, respectively. Red and blue double arrows reveal the directions of maximum and minimum horizontal stress axes, respectively. (For interpretation of the references to colour in this figure legend, the reader is referred to the web version of this article.)

The second mainshock shows a clear SW directivity. The position of the epicenter of the second mainshock relative to the rupture plane (Fig. 8g) indicates a unidirectional rupture towards SW. The distribution of the immediate aftershocks and the damaged villages southwest of the epicenter of the second mainshock further support a SW unidirectional rupture (Fig. 3). For the first mainshock, with its epicenter a few km SW of the second mainshock epicenter, rupture directivity is not clearly resolved but we suggest a unilateral or primarily northeast rupture propagation based on the observed damage distribution that is concentrated NE of its epicenter.

Correlation of the geometry of active faults (Fig. 3) with the source characteristics of the Qotur doublet suggests that the doublet ruptured the full length of the causative fault zone. Fig. 3 shows that the fault zone itself likely consists of several smaller faults. The causative left-lateral strike-slip fault zone does not continue further to the SW. Left-lateral strike-slip faulting does exist SW of the epicentral area but separated from the Qotur area by a gap and with a slightly different strike. At the northern end, conjugate right-lateral strike-slip faults detected by the aftershock alignment limit the northern extent of the rupture plane for the second event. The geometry of the known active fault segments in the remaining unruptured part of the Bashkale fault zone (Fig. 3, i.e., the distance between south of Ravian to the south of Ozpinar) shows no significant disruption (i.e., sudden change in the azimuth or large distance between segments). The simple geometry might allow for full rupture of the unruptured part of the Bashkale fault zone (~ 25 km) and occurrence of an earthquake as large as  $\sim$ 6.5  $M_w$  in the future.

The relative locations do not constrain whether the Qotur doublet and most of its aftershocks ruptured on a single or on multiple fault planes. A single plane scenario would imply that the fault would change dip and also slip with depth with a shallow strike-slip and a deeper oblique-slip part based on the depth differences of the two main shocks. We consider this scenario less likely than slip on two main NE-SW trending and slightly offset faults with slightly different fault strikes and dips. Indirect support for the second scenario comes from the fore- and aftershock moment tensors which are similar to either mainshock focal mechanism though each group spans a wide depth range inconsistent with a single fault model even when considering centroid depth uncertainties. The aftershock distribution also implies activation of additional NW-SE trending strike-slip fault(s).

The observed extensive off-fault aftershock activity (Fig. 3), spatial variability in moment tensors (Fig. 8) and the weakly discernible neotectonic landforms suggest the event doublet ruptured the highly immature crisscrossing Bashkale fault system at the northern end of the more mature Zagros MRF. Mature faults usually are characterized by localized deformation, tight aftershock clouds and larger cumulative surface slip (e.g., Sethanant et al., 2023 and references there) and have more pronounced neotectonic landforms. In contrast, accommodation of strain at the termination of mature faults seems to involve faulting in a complex network of immature faults as seen elsewhere (e.g., Chorsi et al., 2022; Sethanant et al., 2023; Braunmiller and Wetmore, 2024). Due to the width of the off-fault seismicity and the related deformation, the avoidance zone (i.e., an area around an active fault where strong mitigation regulations should be implemented for any future civic developments) for immature fault system should be wide. Additionally, due to low cumulative surface slip and low seismicity, not all branches of complex immature fault systems may be easily detectable making them difficult targets for hazard estimation.

Our stress inversion of moment tensors with significant strike-slip component indicates an NNW-SSE direction of maximum horizontal compression which is in agreement with sinistral and dextral strike-slip movements along NW-SE and NE-SW trending strike-slip faults, respectively, as well as a normal movement component along NNE-SSW trending normal faults. The stress inversion of the earthquakes with dominant normal mechanisms indicate an ENE-WSW direction of the minimum horizontal extension in agreement with the eastward motion of the Iranian Plateau. The focal mechanism of the 1930 Salmas earthquake (Fig. 1b) and the active surface faults (Fig. 3) fully agree with the calculated direction of maximum and minimum horizontal compression.

The interseismic strain tensor in the western Urmia Lake region obtained for 1997 to 2015 indicates an ENE-WSW extensional regime (Khorrami et al., 2019) (Fig. 1a). This finding aligns closely with the ENE-WSW-oriented minimum horizontal stress axis ( $\sigma_3$ ) derived from the stress inversion analysis of moment tensor solutions for recent earthquakes (Figs. 8 and 9). Notably, Niassarifard et al. (2021) report a consistent tensional direction for the regional stress field west and south of Urmia Lake, based on long-term fault-slip data from structural measurements. These consistent long- and short-term results suggest that the modern stress regime has been driven by long-term tectonic adjustments in the region. The stress regime facilitates eastward and westward crustal motion through left- and right-lateral strike-slip fault systems, including the Serow-Bashkale, Chalderan, Derik, Salmas, and northern branches of the Zagros Main Recent Fault.

The Qotur sequence happened close to the boundary between the Iranian Plateau, the Van block, and the Persian block (Fig. 1a). The transtensional tectonic regime in the Bashkale fault system (Niassarifard et al., 2021) is due to differential motion between the Van block and the Iranian Plateau with the Van block moving more northwesterly than the Iranian Plateau and Persian block (Fig. 1a) resulting in a transtensional relative motion between the Van block and the Iranian Plateau. Further north, motion is relative to the Persian block and the direction of the relative motion changes to a right-lateral motion concordant with the NW-SE trending NTG fault system. The Qotur main events and most of its aftershocks happened along the NE-trending boundary between the Iranian Plateau and the Van block. These events have a mostly leftlateral strike-slip mechanisms with variable amounts of normal faulting accommodating ~E-W opening. Our aftershock analysis suggests that the main events also triggered activity on the right-lateral fault systems which mark the boundary between the Van Block and the Persian Block.

Future research aimed at enhancing our understanding of the seismotectonic of the study area could focus on several key approaches. First, expanding the density of the seismic network would improve the quantity and quality of focal mechanism solutions, leading to more accurate stress tensor estimations. Additionally, detailed field measurements of fault kinematic data (i.e., fault planes, striations, and slip sense)

could provide valuable insights into the long-term stress field of the study area. To better assess crustal deformation, installing a dense GPS network would help quantify interseismic strain and establish an upper limit for seismic strain rates. Furthermore, deploying an east-west trending passive seismic profile across the Serow-Bashkale fault zone and its surrounding regions could assess extent of crustal thinning due to ~E-W extension, offering estimates for the duration of ongoing extensional processes. These combined efforts would significantly advance our comprehension of the region's tectonic dynamics and seismic hazards.

#### 6. Conclusions

The 23 February 2020 Qotur earthquake doublet (5.7 and 5.9  $M_{\rm w}$ ) provides critical insights into the complex tectonic processes at the northern termination of the Zagros' Main Recent Fault (MRF) and the interaction between the Iranian Plateau, the Van block, and the Persian block. Our integrated analysis, combining geological fault mapping, precise earthquake relocations, moment tensors, and InSAR source modeling, reveals that the doublet ruptured along NE-SW trending left-lateral strike-slip faults within the Bashkale fault system. However, the seismic cluster also activated conjugate NW-SE trending right-lateral strike-slip faults, highlighting the distributed nature of strain accommodation in this region.

The second mainshock exhibited clear southwest directivity, supported by the spatial distribution of aftershocks and damage patterns, while the first mainshock likely propagated unilaterally to the northeast. The InSAR model for the second mainshock shows a width and length of 7 km and 5 km, respectively, for the fault patch that broke with maximum displacement reaching  $\sim 1.2$  m at  $\sim 3$  km depth. The stress inversion results indicate a transtensional regime with an NNW-SSE direction of maximum horizontal compression, consistent with the focal mechanisms of the 1930 Salmas earthquake and GPS-derived strain directions. This stress regime accommodates the differential motion between the Van block and the Iranian Plateau, with the Van block moving more northwesterly, leading to left-lateral strike-slip faulting with a component of normal faulting along the NE-SW trending faults.

The Qotur doublet ruptured an immature fault system characterized by distributed deformation, off-fault aftershock activity, and weakly discernible neotectonic landforms. This contrasts with mature faults, which typically exhibit localized deformation and pronounced surface expressions. The complex network of immature faults in the region poses significant challenges for seismic hazard assessment, as not all fault branches may be easily detectable due to low cumulative slip and sparse seismicity. Consequently, a wide avoidance zone around active faults is recommended for future development to mitigate seismic risks.

Our findings emphasize the importance of considering the full complexity of fault systems, particularly at the termination of major strike-slip faults like the Zagros MRF. The Qotur sequence underscores the need for detailed seismic monitoring, robust relocation techniques, and integrated geophysical and geological analyses to better understand fault interactions and improve hazard assessments in tectonically active continental collision regions. The potential for future large earthquakes (up to  $\sim\!6.5~M_{\rm w}$ ) along the unruptured segments of the Bashkale fault system highlights existing seismic hazard in this region and the necessity for continued research and preparedness.

#### CRediT authorship contribution statement

Abdolreza Ghods: Writing – review & editing, Writing – original draft, Visualization, Validation, Supervision, Project administration, Methodology, Investigation, Formal analysis, Data curation, Conceptualization. Mahin Jafari: Visualization, Methodology, Formal analysis, Data curation. Jochen Braunmiller: Writing – review & editing, Visualization, Software, Methodology, Investigation, Formal analysis. Mahtab Aflaki: Writing – review & editing, Methodology, Investigation,

Formal analysis. **Eric Bergman:** Writing – review & editing, Software, Methodology, Investigation. **Zahra Mousavi:** Methodology, Data curation. **Esmaeil Farzaneghan:** Data curation. **Andrea Walpersdorf:** Writing – review & editing.

#### Declaration of competing interest

The authors declare that they have no known competing financial interests or personal relationships that could have appeared to influence the work reported in this paper.

# Acknowledgments

The authors thank the Iranian Seismological Center at the Institute of Geophysics, University of Tehran, the Iranian National Seismic Network of the International Institute of Earthquake Engineering and Seismology, the Iran Strong Motion Network of the Building and Housing Research Center and the seismic networks associated with the Disaster and

Emergency Management Presidency of Türkiye (AFAD) and the Kandilli Observatory, Türkiye for providing waveform and/or bulletin and phase data. We also acknowledge seismic waveform data obtained through the IRIS Data Management Center and the Geofon data center. We would like to thank the European Space Agency (ESA) for providing SAR images TOPS S1 which are processed using NSBAS (Marie-Pierre Doin et al., 2011). Most figures were generated using the public license Generic Mapping Tools (GMT) software (Wessel et al., 2019). We also used SRTM DEM derived from the USGS/NASA SRTM data. We utilized open-source geodetic Bayesian Inversion Software (GBIS) released by the Centre for Observation and Modeling of Earthquakes, Volcanoes, and Tectonics (COMET) (Bagnardi and Hooper, 2018). We used a modified version of the open-source software FaultResampler 1.4 to invert for the slip distribution on a fault plane (Barnhart and Lohman, 2010). We thank the associate editor, Dr. Yingfeng Zhang, and one anonymous reviewers for their insightful reviews, which helped us to improve the manuscript.

#### Appendix A. Appendix

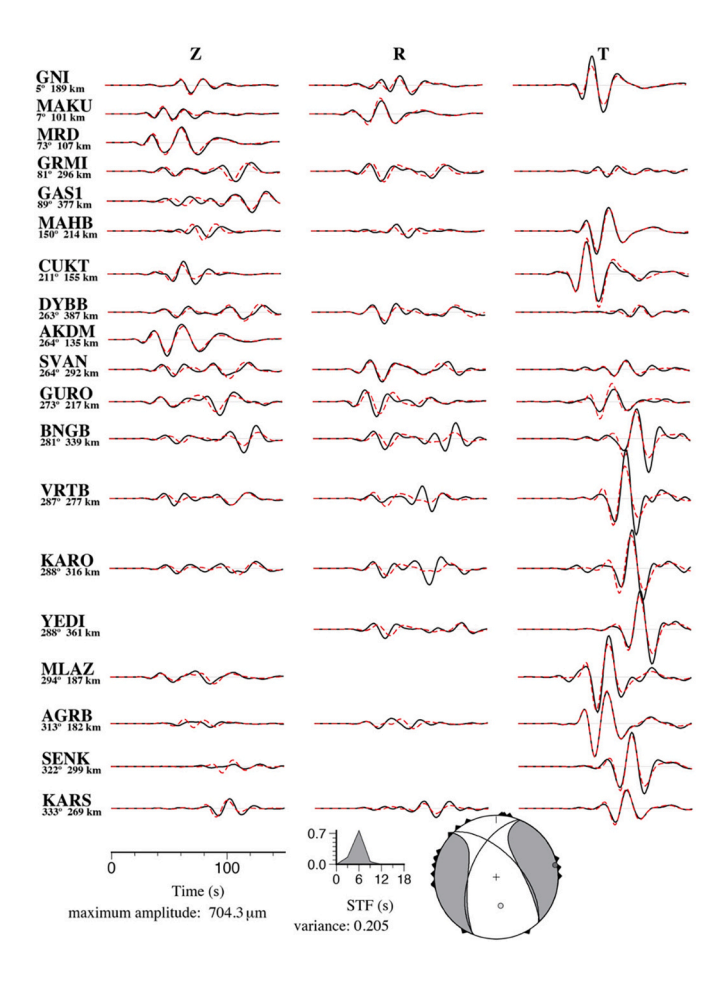


Fig. A1. Waveform fit for the first mainshock (200,223.0552) in the 18–50 s passband for sites within 400 km distance for the best-fitting centroid depth of 9 km. Stations are ordered azimuthally, numbers beneath station codes are event-station azimuth and distance. Black: observed, red dashed: synthetic seismograms. Z, R, and T are vertical, radial, and transverse components, respectively. Triangles on the focal mechanism show the good azimuthal station distributions. (For interpretation of the references to colour in this figure legend, the reader is referred to the web version of this article.)

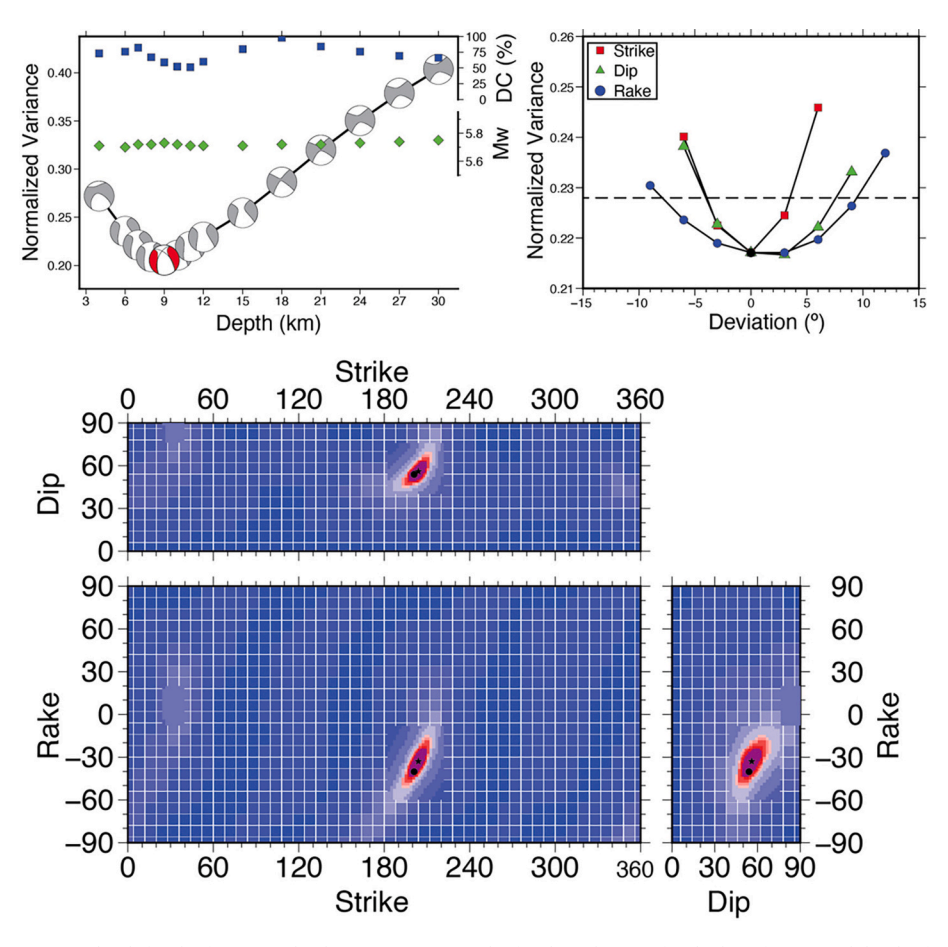


Fig. A2. Top left shows variance vs. depth for the first mainshock (200,223.0552); the focal mechanism for the best-fit centroid depth of 9 km is shown in red. Green diamonds and blue squares show how moment magnitude  $M_w$  and double-couple percentage vary with depth. Top right shows variance relative to the best double couple from the deviatoric moment tensor when modifying one parameter while holding the other fixed (e.g., strike free and dip and rake fixed to best solution values). For a 5 % variance increase (dashed line), strike/dip/rake bounds are approximately  $\pm 4^{\circ}$ ,  $\pm 6^{\circ}$ , and  $\pm 9^{\circ}$ , respectively, but they are not necessarily symmetric relative to the best solution. Bottom shows misfits for a full (nested) double couple grid search. Purple contains solutions with  $\leq 1$  % variance increase and four red-to-pink tones  $\leq 2$  % to  $\leq 5$  %. Black dot is best double couple from deviatoric moment tensor, star is best double couple from constrained double couple search. Note the parameter trade-off. (For interpretation of the references to colour in this figure legend, the reader is referred to the web version of this article.)

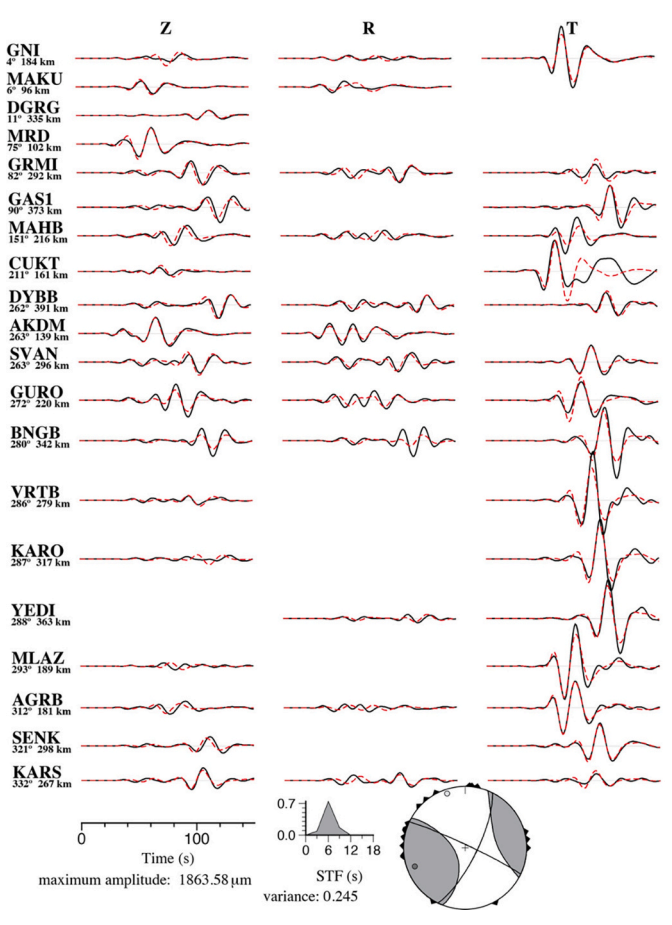


Fig. A3. Waveform fit for the second mainshock (200,223.1600) in the 18–50 s passband for sites within 400 km distance for the best-fitting centroid depth of 5 km. Stations are ordered azimuthally, numbers beneath station codes are event-station azimuth and distance. Black: observed, red dashed: synthetic seismograms. Z, R, and T are vertical, radial, and transverse components, respectively. Triangles on the focal mechanism show the good azimuthal station distributions. (For interpretation of the references to colour in this figure legend, the reader is referred to the web version of this article.)

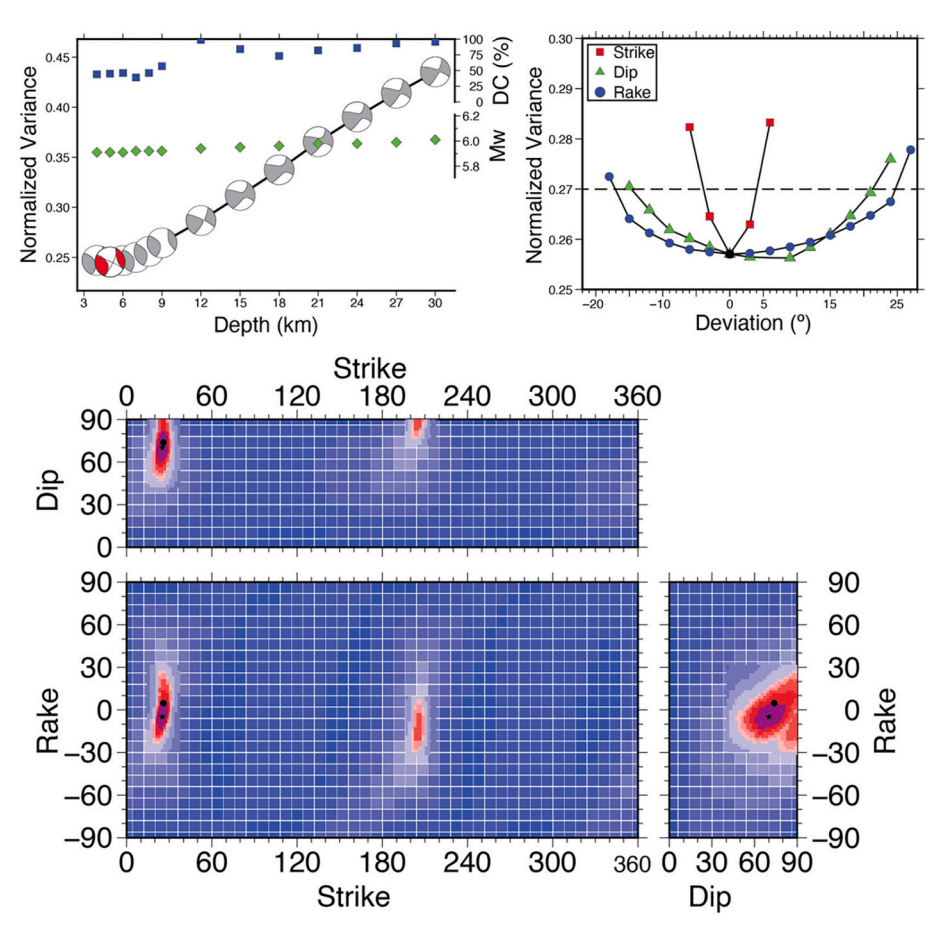


Fig. A4. Same as Fig. A2 but for the second mainshock (200,223.1600) with a centroid depth of 5 km (red focal mechanism). The variance increase away from the best solution with respect to depth, dip and rake is slower than for the first mainshock. This is a typical difference between strike-slip (second mainshock) and dip-slip-to-oblique-slip events (first mainshock); strike is tightly constrained for strike-slip events when the azimuthal coverage is good. For a 5 % variance increase (dashed line top right), strike/dip/rake bounds are approximately  $\pm 4^{\circ}$ ,  $\pm 18^{\circ}$ , and  $\pm 21^{\circ}$ , respectively. The full double couple grid search (at bottom) shows the strong trade-off between dip and rake. (For interpretation of the references to colour in this figure legend, the reader is referred to the web version of this article.)

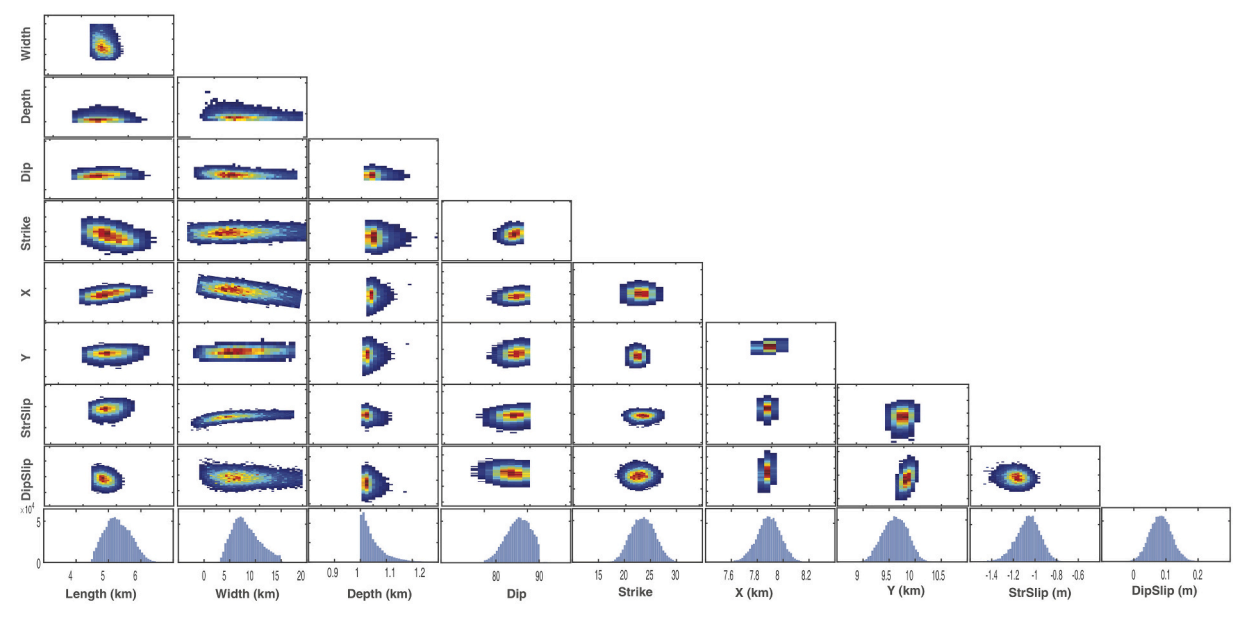


Fig. A5. Scattergrams of the joint probability distributions for the different parameters used in the InSAR constant slip modeling of the second mainshock. The red colour shows the region with the best solution. Panels in the bottom row shows histograms of posterior probability distribution of the estimated parameters indicating a well-resolved solution. StrSlip and DipSlip stands for strike slip and dip slip displacement, respectively. (For interpretation of the references to colour in this figure legend, the reader is referred to the web version of this article.)

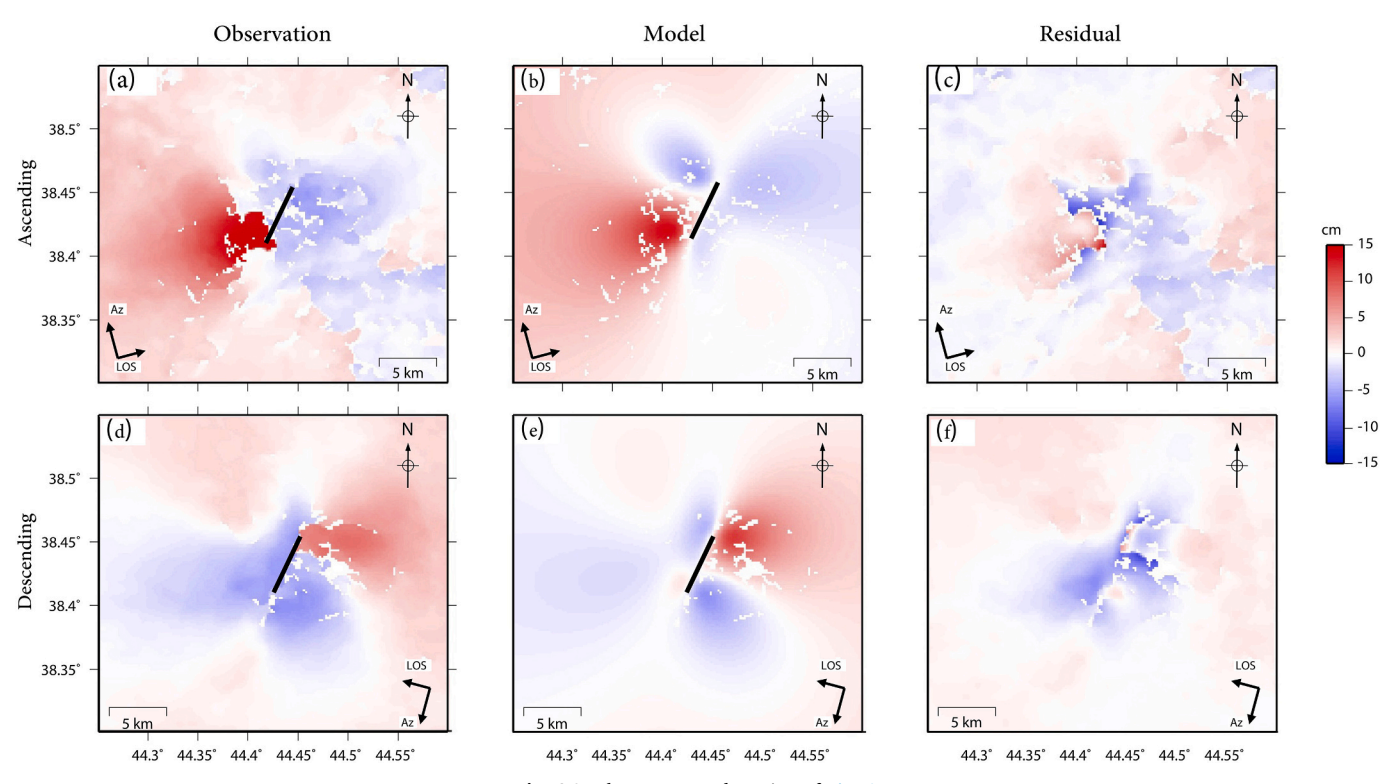


Fig. A6. The unwrapped version of Fig. 6.

Table A1
Calibrated epicenters of the Qotur seismic cluster. Eq. No. is the associated earthquake number in the cluster. Time is given in UTC and Lat. and Lon. are latitude and longitude in degrees N and E. Depth is in kilometer, codes in the D column describe the type of depth constraint: *n* for near-source station readings, l for regional readings, and *c* for cluster-default (fixed) solutions. Mag is the magnitude taken from the ISC bulletin followed by magnitude type. Horizontal location uncertainties are given by the 90 % confidence ellipse with A1 and A2 the azimuths, in degrees clockwise from north, and L1 and L2 the semi-axis lengths in km. The Area column gives the area of the 90 % confidence ellipse in km².

EQ. No.	Date	Time	Lat	Long	Depth (km)	D	Mag	A1	L1	A2	L2	Area (km²)
1	20,090,225	17:28:50.9	38.50799	44.35759	4	1	3.6mb	299	1.44	29	2.56	11.5
2	20,170,326	11:37:59.6	38.47683	44.44447	7	1	3.7mb	293	1.42	23	2.24	10
3	20,191,119	0:14:10.53	38.48713	44.4264	15	1	4.8mb	292	1.27	22	2.24	8.9
4	20,200,216	18:02:12.29	38.46395	44.43729	12	1	4.2ML	290	1.31	20	2.29	9.4
5	20,200,216	18:37:45.14	38.49343	44.4618	10	c	3.5ML	292	1.4	22	2.28	10
6	20,200,218	10:56:20.88	38.45715	44.44128	10	c	2.7ML	290	1.37	20	2.4	10.3
7	20,200,218	19:41:48.66	38.45189	44.4441	10	c	3.7ML	291	1.4	21	2.36	10.4
8	20,200,223	5:42:27.49	38.45071	44.4357	10	c	3.0ML	284	1.53	14	2.83	13.6
9	20,200,223	5:52:57.71	38.4283	44.43057	10	n	5.9 MW	290	1.27	20	2.41	9.6
10	20,200,223	6:00:22.86	38.44487	44.45474	11	n	2.4ML	297	1.48	27	3.07	14.3
11	20,200,223	6:16:39.89	38.43975	44.45395	10	n	3.3ML	290	1.44	20	2.6	11.8
12	20,200,223	6:22:54.88	38.42614	44.46569	7	n	2.7ML	290	1.36	20	2.43	10.4
13	20,200,223	6:31:21.32	38.47542	44.45161	10.5	n	3.7ML	289	1.4	19	2.41	10.6
14	20,200,223	6:34:41.16	38.4198	44.45877	10	n	2.7ML	290	1.53	20	2.79	13.4
15	20,200,223	6:40:37.13	38.45062	44.44539	10	n	2.3ML	291	1.72	21	3	16.2
16	20,200,223	6:52:13.79	38.43903	44.4717	10	c	1.9ML	300	1.58	30	2.73	13.6
17	20,200,223	7:07:49.59	38.50192	44.47109	10	c	1.9ML	303	2.24	33	3.51	24.7
18	20,200,223	7:16:5.93	38.48032	44.42619	10	c	3.9 MW	292	1.41	22	2.49	11
19	20,200,223	7:50:46.99	38.41787	44.42233	10	c	4.0 MW	290	1.3	20	2.29	9.4
20	20,200,223	7:55:48.44	38.4234	44.42422	10	c	2.9ML	291	1.55	21	2.61	12.7
21	20,200,223	8:21:55.11	38.42495	44.46856	10	c	2.7ML	291	1.37	21	2.39	10.3
22	20,200,223	8:28:48.47	38.41438	44.40582	10	c	2.9ML	291	1.46	21	2.5	11.5
23	20,200,223	8:39:04.15	38.38944	44.42987	10	c	2.5ML	287	1.7	17	2.95	15.7
24	20,200,223	9:07:29.8	38.48756	44.41125	10	c	2.5ML	292	1.43	22	2.52	11.3
25	20,200,223	9:28:31.55	38.47647	44.43317	10	c	2.5ML	293	1.41	23	2.42	10.8
26	20,200,223	9:48:20.61	38.44907	44.45699	10	c	4.4 MW	291	1.26	21	2.28	9
27	20,200,223	10:06:05.3	38.46043	44.4463	10	c	3.9 MW	291	1.38	21	2.38	10.4
28	20,200,223	10:25:37.77	38.4492	44.44046	10	c	3.9ML	291	1.28	21	2.26	9.1
29	20,200,223	10:29:34.33	38.47052	44.42253	10	c	3.9ML	292	1.31	22	2.33	9.6
30	20,200,223	10:50:56.55	38.47974	44.42085	10	c	3.2ML	289	1.43	19	2.63	11.8
31	20,200,223	11:01:03.2	38.45432	44.43858	10	c	3.0ML	291	1.34	21	2.41	10.2

(continued on next page)

Table A1 (continued)

EQ. No.	Date	Time	Lat	Long	Depth (km)	D	Mag	A1	L1	A2	L2	Area (km²)
32	20,200,223	11:14:44.83	38.43817	44.44346	10	c	3.2ML	291	1.37	21	2.37	10.2
33	20,200,223	11:36:35.71	38.45258	44.46357	10	c	2.9ML	296	1.84	26	2.89	16.7
34 35	20,200,223 20,200,223	11:57:53.16	38.43721 38.43065	44.44775	10 10	c	3.0ML 2.7ML	294 294	1.34	24	2.44	10.3
36	20,200,223	12:06:48.65 14:25:48.53	38.4954	44.44536 44.45697	10	c c	2.7ML 2.7ML	294	1.5 1.4	24 23	2.45 2.39	11.5 10.5
37	20,200,223	14:28:37.74	38.39909	44.40829	10	c	4.3 MW	290	1.33	20	2.37	9.9
38	20,200,223	16:00:28.24	38.454	44.451	10	c	6.0 MW	290	1.26	20	2.26	8.9
39	20,200,223	16:10:55.21	38.5001	44.46909	10	c	3.4ML	293	1.7	23	2.92	15.6
40	20,200,223	16:13:52.23	38.43344	44.44949	10	c	3.5ML	291	1.5	21	2.56	12.1
41	20,200,223	16:16:17.67	38.46564	44.4551	10	c	3.1ML	294	1.36	24	2.39	10.2
42	20,200,223	16:20:16.53	38.45659	44.47849	10	c	3.6ML	290	1.39	20	2.45	10.7
43	20,200,223	16:24:52.79	38.43981	44.42692	10	c	3.5ML	292	1.36	22	2.33	10
44	20,200,223	16:37:49.71	38.45923	44.45769	10	c	3.6ML	291	1.29	21	2.28	9.2
45	20,200,223	16:39:56.59	38.43536	44.46057	10	c	3.9ML	291	1.3	21	2.36	9.6
46	20,200,223	16:54:36.52	38.45963	44.41933	10	c	4.0ML	292	1.29	22	2.33	9.4
47	20,200,223	16:56:20.27	38.46595	44.42206	10	c	4.4 MW	288	1.36	18	2.45	10.5
48	20,200,223	17:00:39.92	38.48454	44.45739	10	c	3.6ML	291	1.42	21	2.52	11.3
49	20,200,223	17:07:22.21	38.43095	44.42193	10	c	3.5ML	291	1.37	21	2.66	11.5
50	20,200,223	17:10:37.73	38.43143	44.46016	10	c	3.4ML	292	1.27	22	2.39	9.5
51	20,200,223	17:21:57.57	38.43629	44.40499	10	c	3.7 MW	291	1.31	21	2.35	9.6
52	20,200,223	18:12:47.7	38.39657	44.40617	10	c	3.4ML	295	1.39	25	2.44	10.7
53	20,200,223	18:25:45.83	38.38068	44.39207	10	c	3.6ML	289	1.33	19	2.36	9.9
54	20,200,223	18:33:21.16	38.42291	44.43779	10	c	3.4ML	296	1.38	26	2.47	10.7
55	20,200,223	18:35:22.31	38.43333	44.43419	10	c	2.5ML	292	1.37	22	2.49	10.7
56	20,200,223	18:48:27.33	38.44186	44.40754	10	c	2.9ML	292	1.38	22	2.4	10.4
57	20,200,223	19:42:37.39	38.43583	44.4455	10	c	3.5ML	291	1.33	21	2.32	9.7
58	20,200,223	19:57:32.78	38.37607	44.41422	10	c	2.6ML	292	1.47	22	2.74	12.6
59	20,200,223	20:44:35.89	38.40779	44.41077	10	c	3.9 MW	293	1.28	23	2.26	9
60	20,200,223	20:55:09.36	38.46573	44.43005	10	c	3.1ML	294	1.25	24	2.25	8.8
61 62	20,200,223	20:57:34.33	38.46062	44.43372 44.40219	10	c	3.4ML	294 290	1.29	24	2.32 2.47	9.4
63	20,200,223 20,200,223	21:02:14.69 21:33:53.02	38.39843 38.39144	44.41515	10 10	c	3.1ML 2.5ML	293	1.42 1.54	20 23	2.47	11.1 13.4
64	20,200,223	21:36:57.91	38.43353	44.41946	10	c c	2.5ML 2.7ML	293	1.44	23 21	2.78	12.6
65	20,200,223	21:53:02.03	38.42865	44.45695	10	c	2.7ML 2.9ML	292	1.44	22	2.76	11.6
66	20,200,223	22:17:22.03	38.47574	44.45761	10	c	2.9ML	292	1.33	22	2.41	10.1
67	20,200,223	22:30:24.36	38.42108	44.41818	10	c	2.7ML	292	1.53	22	2.74	13.2
68	20,200,223	22:36:38.69	38.49933	44.28886	10	c	3.2ML	292	1.39	22	2.41	10.5
69	20,200,224	0:10:39.57	38.44264	44.49148	10	c	2.6ML	294	1.43	24	2.62	11.8
70	20,200,224	0:16:21.14	38.45738	44.42445	10	c	2.8ML	292	1.4	22	2.49	11
71	20,200,224	0:50:42.03	38.46105	44.45749	10	c	3.2ML	291	1.43	21	2.48	11.2
72	20,200,224	1:00:32.7	38.44197	44.44878	10	c	2.9ML	294	1.49	24	2.57	12
73	20,200,224	1:32:35.58	38.42849	44.42852	10	c	2.6ML	289	1.45	19	2.51	11.4
74	20,200,224	1:45:55.31	38.39187	44.41949	10	c	2.5ML	294	1.58	24	2.65	13.2
75	20,200,224	1:54:30.5	38.42438	44.44814	10	c	2.8ML	290	1.43	20	2.51	11.3
76	20,200,224	3:29:36.33	38.43182	44.47572	10	c	3.0ML	292	1.43	22	2.51	11.3
77	20,200,224	4:40:50.82	38.37178	44.40084	10	c	2.6ML	292	1.66	22	2.4	12.5
78	20,200,224	5:19:17.08	38.40024	44.40945	10	c	3.0ML	285	1.52	15	2.76	13.2
79	20,200,224	8:53:08.52	38.48261	44.4812	10	c	4.0 MW	292	1.54	22	2.37	11.4
80	20,200,224	8:58:12.75	38.46375	44.38758	10	c	2.9ML	292	1.37	22	2.25	9.7
81	20,200,224	15:05:36.38	38.39576	44.39632	10	c	3.7ML	292	1.48	22	2.34	10.8
82	20,200,224	16:02:37.17	38.4454	44.44395	10	c	3.4ML	293	1.34	23	2.35	9.9
83	20,200,224	16:32:52.68	38.4712	44.37352	10	c	3.0ML	294	1.52	24	2.36	11.2
84	20,200,224	17:05:00.09	38.3885	44.38803	10	c	3.7 MW	292	1.37	22	2.33	10.1
85	20,200,224	23:44:34.33	38.46581	44.39896	10	c	3.8ML	293	1.34	23	2.23	9.4
86	20,200,225	0:08:27.46	38.46362	44.35517	10	c	3.8 MW	292	1.28	22	2.26	9.1
87	20,200,225	0:22:20.97	38.43582	44.46022	10	С	2.5ML	290	1.44	20	2.45	11.1
88	20,200,225	6:32:19.2	38.48063	44.38246	10	c	2.7ML	293	2.14	23	3.31	22.3
89	20,200,225	7:13:56.9	38.46444	44.38373	10	c	2.7ML	290	1.52	20	2.64	12.6
90	20,200,225	9:40:31.14	38.41491	44.41247	10	c	3.6 MW	287	1.6	17	2.71	13.6
91	20,200,225	12:30:30.18	38.46332	44.46593	10	c	3.4ML	287	1.62	17	3.37	17.2
92	20,200,225	12:39:48.51	38.42296	44.47416	10	c	2.5ML	295	1.57	25	2.65	13
93 94	20,200,225 20,200,225	13:42:29.26 14:14:01.79	38.38378 38.46724	44.40168 44.41858	10 10	c c	3.2ML 4.1ML	296 292	1.88 1.28	26 22	3.06 2.22	18.1 8.9
95	20,200,225	14:40:37.07	38.46553	44.42648	10	c	2.5ML	292	1.26	22	2.32	11
96	20,200,225	15:09:10.44	38.45227	44.43293	10	c	2.5ML	292	1.53	21	2.48	11.9
97	20,200,225	15:19:11.23	38.46729	44.36796	10	c	2.5ML	297	1.76	27	2.46	13.1
98	20,200,225	15:43:51.68	38.44258	44.4364	10	c	2.5ML	273	2.35	3	3.17	23.4
98	20,200,225	15:58:20.00	38.48948	44.46674	10	c	3.3ML	2/3 292	1.33	3 22	2.24	9.3
100	20,200,225	22:28:11.75	38.47842	44.3768	10	c	4.0ML	292	1.33	22	2.3	9.6
100	20,200,226	4:26:50.33	38.42078	44.44086	10	c	3.7ML	288	1.36	18	2.45	10.5
102	20,200,226	23:32:04.92	38.41275	44.41269	10	c	2.6ML	289	1.34	19	2.32	9.8
103	20,200,227	2:36:47.08	38.46611	44.40941	10	c	2.6ML	287	1.41	17	2.39	10.6
103	20,200,227	9:24:04.95	38.51284	44.46868	10	c	2.8ML	300	1.72	30	2.85	15.4
105	20,200,227	13:20:12.98	38.4407	44.43763	10	c	2.8ML	289	1.6	19	3.48	17.5
	20,200,227	14:56:22.49	38.4596	44.40705	10	c	3.6ML	292	1.26	22	2.28	9

(continued on next page)

Table A1 (continued)

EQ. No.	Date	Time	Lat	Long	Depth (km)	D	Mag	A1	L1	A2	L2	Area (km²)
107	20,200,227	15:11:54.21	38.38934	44.43022	10	c	2.5ML	293	1.39	23	2.37	10.3
108	20,200,227	19:52:12.69	38.44265	44.45855	10	c	3.1ML	291	1.44	21	2.45	11.1
109	20,200,228	4:27:46.23	38.41473	44.41434	10	c	2.7ML	292	1.55	22	2.7	13.1
110	20,200,228	6:52:35.09	38.40217	44.37007	10	c	2.5ML	272	2.34	2	2.9	21.3
111	20,200,228	11:55:19.02	38.35175	44.45235	10	c	2.5ML	89	1.98	179	3.35	20.8
112	20,200,228	13:57:11.79	38.52663	44.49833	10	c	2.8ML	291	1.39	21	2.74	12
113	20,200,228	14:34:34.85	38.49287	44.44374	10	c	2.7ML	289	1.37	19	2.39	10.3
114	20,200,228	18:29:12.22	38.43032	44.42609	10	c	2.6ML	291	1.33	21	2.34	9.8
115	20,200,229	0:05:45.71	38.48586	44.43856	10	c	3.7 MW	291	1.37	21	2.4	10.3
116	20,200,229	0:57:23.91	38.44023	44.42268	10	c	2.5ML	292	1.31	22	2.31	9.5
117	20,200,229	1:39:50.9	38.43247	44.40425	10	c	2.7ML	291	1.44	21	2.49	11.2
118	20,200,229	11:19:43.38	38.40435	44.41029	10	c	3.3ML	294	1.37	24	2.35	10.1
119	20,200,229	12:49:51.15	38.49107	44.33119	11.5	n	2.6ML	68	2.28	158	2.76	19.7
120	20,200,303	0:13:44.34	38.4542	44.40549	10	c	2.7ML	292	1.4	22	2.48	10.9
121	20,200,303	16:25:32.41	38.55512	44.49009	10	c	2.8ML	293	1.45	23	2.28	10.4
122	20,200,304	11:33:44.45	38.38689	44.42838	10	c	3.9ML	293	1.37	23	2.47	10.6
123	20,200,304	14:40:54.4	38.37758	44.42307	10	c	3.2ML	292	1.49	22	2.28	10.7
124	20,200,304	17:28:30.44	38.38478	44.42485	13	n	3.2ML	290	1.42	20	2.25	10
125	20,200,305	6:12:27.1 6:34:05.22	38.49988	44.43719	10	c	2.5ML	293	1.49	23	2.32	10.9
126	20,200,305		38.45512	44.43707	7	n	2.5ML	292	1.26	22	2.36	9.3
127	20,200,306 20,200,306	10:38:57.21	38.51189	44.33841	14	n	3.5ML	291	1.77	21	2.83	15.8
128		14:19:46.58	38.51333	44.31557	13	n	4.4 MW	295	1.48	25	2.34	10.9
129	20,200,307	0:06:33.36	38.51384	44.46749	10	n	3.6ML	286	1.56	16	2.63	12.9
130	20,200,307	13:38:03.84	38.45827	44.45092	10	c	3.1ML	291	1.61	21	2.35	11.9
131	20,200,307	18:45:13.02	38.49397	44.43079	13.5	n	2.9ML	281	1.68	11	2.58	13.7
132	20,200,309	17:24:37.54	38.48282	44.39584	7.5	n	2.5ML	292	1.4	22	2.3	10.1
133	20,200,310	2:53:47.36	38.41362	44.43707	10.5	n	3.7ML	292	1.35	22	2.48	10.5
134	2,020,310	13:03:40.62	38.46146	44.46266	9.7	n	3.1ML	291	1.54	21	2.36	11.4
135	20,200,311	7:29:38.76	38.50943	44.34291	10	c	2.9ML	293	1.65	23	2.82	14.6
136	20,200,311	9:36:52.02	38.52665	44.35123	11.2	n	3.0ML	291	1.55	21	2.65	12.9
137	20,200,311	10:43:06.39	38.42376	44.50496	8.5	n	3.2ML	293	1.32	23	2.28	9.5
138	20,200,311	11:36:14.98	38.44262 38.4313	44.47104 44.46029	10	c	2.9ML	292 292	1.4	22	2.28 2.37	10
139 140	20,200,312	22:24:32.31		44.49558	8	n	2.8ML	292 291	1.47 1.52	22 21	2.32	11 11.1
140	20,200,313 20,200,316	16:20:24.18 7:05:59.05	38.42735 38.43565	44.40839	10 10	c	2.6ML 2.5ML	291	1.52	23	2.34	
141	20,200,316	23:07:19.44	38.49889	44.47043	10	c	3.9ML	293 286	1.62	23 16	2.57	11.4 13.1
142		7:13:53.48	38.5695	44.47274	10	c	3.7ML	292	1.46	22	2.42	11.1
143	20,200,319 20,200,319	10:25:10.45	38.4628	44.44386	10	c	3.7ML 3.1ML	292	1.46		2.42	11.1
						c				25		
145	20,200,320	11:12:57.51	38.47145	44.46011	10 10	c	3.0ML	294 287	1.57 1.49	24	2.31	11.3
146	20,200,321	0:41:26.98	38.45911	44.43745 44.37854		c	2.5ML	287 292	1.49	17	2.37 2.7	11.1 12.6
147 148	20,200,321 20,200,321	16:08:51.48 22:41:32.11	38.39915 38.3439	44.37854	10 10	c c	2.7ML 3.5ML	292	1.49	22 22	2.77	12.6
149	20,200,321	3:29:33.5	38.47042	44.45065	10	c	2.7ML	293	1.53	23	2.22	10.7
150	20,200,322	14:06:08.67	38.51044	44.30003	12	n	2.7ML 2.5ML	293	1.68	22	2.61	13.7
150	20,200,323	18:10:24.11	38.42972	44.39821	10	c	2.5ML	292	1.72	21	3.26	17.6
151	20,200,323	18:58:12.48	38.47882	44.459	10	c	2.8ML	291	1.61	24	2.36	12.0
152	20,200,324	12:05:54.55	38.48974	44.51879	10	c	2.9ML	294	1.56	20	2.59	12.7
153	20,200,325	23:18:05.27	38.4526	44.46044	10	c	2.9ML	293	1.47	23	2.39	10.6
155	20,200,325	5:39:16.61	38.44103	44.51477	10	c	4.1ML	293	1.47	23	2.59	11.5
156	20,200,326	12:59:42.03	38.44005	44.4488	10	c	2.8ML	293	1.51	23	2.51	11.9
157	20,200,326	20:34:37.72	38.46727	44.42171	10	c	3.0ML	299	1.69	29	2.31	12.3
158	20,200,403	9:42:44.2	38.48674	44.3741	10		4.0ML	295	1.49	25	2.31	10.8
159			38.34875	44.2874	10	c	3.7 MW	295	1.55		2.34	11.4
	20,200,408	20:43:31.06		44.40034		c				25		
160	20,200,411 20,200,412	17:52:43.3 2:23:09.16	38.38981 38.45564	44.41072	10	c	2.5ML 4.0ML	280 290	1.69 1.28	10	4.08	21.6 9.7
161 162	20,200,412 20,200,417	2:23:09.16 10:11:47.87	38.45564 38.38272	44.41072	10 10	c	4.0ML 2.8ML	290 295	1.28	20 25	2.4 3.43	9.7 18
		21:07:04.27		44.3888		n	3.8 MW					
163	20,200,420		38.45648		11.5	n		295	1.52	25	2.31	11
164	20,200,423	6:46:18.27	38.5134	44.48306	7.5	n	3.8 MW	284	1.36	14	3.06	13.1
165	20,200,424	19:47:10.86	38.3768	44.38906	10	c	2.5ML	285	1.56	15	2.55	12.5
166	20,200,429	19:33:16.83	38.41523	44.43353	10	c	3.4ML	292	1.45	22	2.69	12.2
167	20,200,501	12:08:46.62	38.40483	44.46864	10	c	3.6 MW	284	1.61	14	2.48	12.5
168	20,200,502	8:41:21.16	38.52876	44.46117	10	c	4.0 MW	290	1.42	20	2.62	11.7
169	20,200,509	7:20:31.31	38.45249	44.37967	10	c	2.9ML	9	2.13	99	2.18	14.6

Table A2 30 moment tensor solutions calculated in this study. Depth, strike, dip, rake,  $M_w$  and Q are from moment tensor analysis. Solution and centroid quality (Q) classes A/B/C are based on normalized variance  $\le 0.3$ ,  $\le 0.4$ , > 0.4, and depth uncertainty  $\le \pm 4$  km,  $\le \pm 8$  km,  $> \pm 8$  km, F is fixed, respectively. Row 31 is the focal mechanism for the 1930 Salmas earthquake from Jackson and McKenzie (1988) with location from the ISC-GEM catalog (Storchak et al., 2013; Storchak et al., 2015; Di Giacomo et al., 2018).

No.	Date	Time (UTC)	Lat.	Long.	Depth	Strikeeeedeeee	Dip	Rake	Mw	Q
-		<del></del>					_			_

(continued on next page)

Table A2 (continued)

No.	Date	Time (UTC)	Lat.	Long.	Depth	Strikeeeedeeee	Dip	Rake	Mw	Q
	(yyyy.mm.dd)	(hh:mm)	(°N)	(°E)	(km)					
	(yyyy.mm.dd)	(hh:mm)	(°N)	(°E)	(km)					
1	2020.02.16	18:02	38.46395	44.43729	5	321	48	-105	4.45	A/A
2	2020.02.18	19:41	38.45189	44.44410	8	317	52	-119	4.01	B/A
3	2020.02.23	5:52	38.42830	44.43057	9	317	58	-137	5.73	A/A
4	2020.02.23	7:50	38.41787	44.42233	11	214	75	-23	4.18	B/A
5	2020.02.23	9:48	38.42265	44.49916	8	307	51	-129	4.22	A/A
6	2020.02.23	10:06	38.46043	44.44630	8	41	71	-8	3.92	B/A
7	2020.02.23	10:25	38.44920	44.44046	9	41	86	13	4.16	A/A
8	2020.02.23	14:28	38.39909	44.40829	11	38	42	-30	4.11	B/B
9	2020.02.23	16:00	38.45400	44.45100	5	26	74	5	5.91	A/A
10	2020.02.23	16:54	38.45963	44.41933	8	196	84	-10	4.33	B/C
11	2020.02.23	16:56	38.46595	44.42206	10	196	81	-14	4.27	C/B
12	2020.02.23	17:00	38.48454	44.45739	9	20	77	-23	4.90	C/F
13	2020.02.23	20:44	38.40779	44.41077	12	42	58	-9	3.97	B/F
14	2020.02.24	8:53	38.48261	44.48120	5	176	52	-67	3.87	C/A
15	2020.02.24	15:05	38.39576	44.39632	11	33	74	3	4.31	A/A
16	2020.02.24	23:44	38.46581	44.39896	7	60	58	-6	4.19	A/A
17	2020.02.25	13:42	38.38378	44.40168	6	213	35	-20	3.78	C/B
18	2020.02.25	14:14	38.46724	44.41858	8	26	72	4	4.53	A/B
19	2020.02.25	22:28	38.47842	44.37680	4	23	73	15	4.22	A/B
20	2020.03.04	11:33	38.38689	44.42838	14	27	80	4	4.07	A/B
21	2020.03.06	14:19	38.51333	44.31557	4	40	53	-9	4.45	A/A
22	2020.03.10	2:53	38.41362	44.43707	7	215	41	-24	4.10	A/A
23	2020.03.18	23:07	38.49889	44.47043	8	191	64	-54	4.29	B/B
24	2020.03.19	7:13	38.5695	44.47274	3	190	73	-63	4.07	B/A
25	2020.03.26	5:39	38.44103	44.51477	5	36	55	0	4.41	A/B
26	2020.04.03	9:42	38.48674	44.3741	20	200	75	-23	4.32	A/B
27	2020.04.12	2:23	38.45564	44.41072	7	227	86	-5	4.67	A/A
28	2020.04.20	21:07	38.45648	44.38880	9	49	84	-1	3.95	C/B
29	2020.04.23	6:46	38.51340	44.48306	5	164	42	-68	3.72	C/A
30	2020.05.02	8:41	38.52876	44.46117	6	176	74	-70	3.97	A/F
31	1930.05.06	22:34	38.108	44.727	15	300	40	-140	7.1	-/F

#### Appendix B. Supplementary data

Supplementary data to this article can be found online at https://doi.org/10.1016/j.tecto.2025.230899.

# Data availability

Data will be made available on request.

#### References

- Abdulnaby, W., Al-Mohmed, R., Mahdi, M., 2016. Seismicity and recent stress regime of Diyala City, Iraq–Iran border. Model. Earth Syst. Environ. 2, 1–8. Springer.
- Aflaki, M., Mousavi, Z., Ghods, A., Shabanian, E., Vajedian, S., Akbarzadeh, M., 2019. The 2017 Mw 6 Sefid Sang earthquake and its implication for the geodynamics of NE Iran. Geophys. J. Int. 218, 1227–1245. https://doi.org/10.1093/gji/ggz172.
- Aflaki, Mahtab, Shabanian, E., Sahami, S., Arshadi, M., 2021. Evolution of the stress field at the junction of Talesh Alborz Central Iran during the past 5 Ma: implications for the tectonics of NW Iran. Tectonophysics 821, 229115. https://doi.org/10.1016/j.tecto.2021.229115.
- Afra, M., Moradi, A., Pakzad, M., 2017. Stress regimes in the northwest of Iran from stress inversion of earthquake focal mechanisms. J. Geodyn. 111, 50–60.
- Ambraseys, N.N., 2009. Earthquakes in the Mediterranean and Middle East. Cambridge University Press.
- Authemayou, C., Chardon, D., Bellier, O., Malekzadeh, Z., Shabanian, E., Abbassi, M.R., 2006. Late Cenozoic partitioning of oblique plate convergence in the Zagros foldand-thrust belt (Iran). Tectonics 25, 1–21. https://doi.org/10.1029/2005TC001860.
- Bagnardi, M., Hooper, A., 2018. Inversion of surface deformation data for rapid estimates of source parameters and uncertainties: a Bayesian approach. Geochem. Geophys. Geosyst. 19, 2194–2211.
- Barnhart, W.D., Lohman, R.B., 2010. Automated fault model discretization for inversions for coseismic slip distributions. J. Geophys. Res. Solid Earth 115.
- Berberian, M., 2014. Patterns of historical earthquake ruptures on the Iranian plateau. Dev. Earth Surf. Process. 17, 439–518. https://doi.org/10.1016/B978-0-444-63292-0.00016-8.
- Berberian, M., Tchalenko, J.S., 1976. Field study and documentation of the 1930 Salmas (Shahpur-Azarbaidjan) earthquake. Geol. Surv. Iran 39, 271–342.
- Berberian, M., Yeats, R., 1999. Patterns of historical earthquake rupture in the Iranian Plateau. Bull. Seismol. Soc. Am. 89, 120–139.

- Bergman, E.A., Benz, H.M., Yeck, W.L., Karasözen, E., Engdahl, E.R., Ghods, A., Hayes, G. P., et al., 2022. A Global Catalog of Calibrated Earthquake Locations. https://doi.org/10.1785/0220220217.
- Braunmiller, J., Ghods, A., 2021. The 2004-2020 Iran moment tensor database from incountry regional broadband data. AGU Fall Meet. Abstr. 2021, S45E–0342.
- Braunmiller, J., Wetmore, P., 2024. The 2020 Mw 6.5 Stanley, Idaho, earthquake and Aftershock Sequence: complex Faulting at the Northern end of the Basin and Range Province. Bull. Seismol. Soc. Am. https://doi.org/10.1785/0120230297.
- Braunmiller, J., Nabelek, J., Ghods, A., 2020. Sensor orientation of Iranian broadband seismic stations from P-wave particle motion. Seismol. Res. Lett. 91, 1660–1671. https://doi.org/10.1785/0220200019.
- Büyükakpinar, P., Aktar, M., Petersen, G.M., Köseöuglu, A., 2021. Orientations of broadband stations of the KOERI seismic network (Turkey) from two independent methods: P-and Rayleigh-wave polarization. Seismol. Res. Lett. 92, 1512–1521.
- Carey-Gailhardis, E., Mercier, J.L., 1987. A numerical method for determining the state of stress using focal mechanisms of earthquake populations: application to Tibetan teleseisms and microseismicity of Southern Peru. Earth Planet. Sci. Lett. 82, 165–179.
- Chorsi, T.S., Braunmiller, J., Deng, F., Dixon, T.H., 2022. Afterslip From the 2020 M 6 . 5 Monte Cristo Range, Nevada Earthquake. Geophys. Res. Lett. 1–10. https://doi.org/ 10.1029/2022GL099952.
- Di Giacomo, D., Engdahl, E.R., Storchak, D.A., 2018. The ISC-GEM earthquake catalogue (1904–2014): status after the extension project. Earth Syst. Sci. Data 10, 1877–1899. Copernicus Publications Göttingen, Germany.
- Doin, M.-P., Lasserre, C., Peltzer, G., Cavalié, O., Doubre, C., 2009. Corrections of stratified tropospheric delays in SAR interferometry: validation with global atmospheric models. J. Appl. Geophys. 69, 35–50.
- Doin, Marie-Pierre, Guillaso, S., Jolivet, R., Lasserre, C., Lodge, F., Ducret, G., Grandin, R., 2011. Presentation of the small baseline NSBAS processing chain on a case example: The Etna deformation monitoring from 2003 to 2010 using Envisat data. Proc. Fringe Symp. 3434–3437.
- Esmaeili, C., Khoush Zare, T., Sartipi, A., Rajebzadeh, H., Nourian, Y., Orouji, Y., 2020.
  Preliminary report of geological investigation of the 23 Feb. 2020 doublet event with magnitudes 5.7 and 5.9 in Ghtour-Western Azerbaijan-Iran (In persian). Geol. Surv. Iran 1–28.

Farr, T.G., Kobrick, M., 2000. Shuttle radar topography mission produces a wealth of data. EOS Trans. Am. Geophys. Union 81, 583–585.

- Ghods, A., Rezapour, M., Bergman, E., Mortezanejad, G., Talebian, M., 2012. Relocation of the 2006 M w 6.1 silakhour, Iran, earthquake sequence: details of fault segmentation on the main recent fault. Bull. Seismol. Soc. Am. 102. https://doi.org/ 10.1785/0120110009.
- Ghods, Abdolreza, Shabanian, E., Bergman, E., Faridi, M., Donner, S., Mortezanejad, G., Aziz-Zanjani, A., 2015. The Varzaghan-Ahar, Iran, Earthquake Doublet (Mw 6.4, 6.2): implications for the geodynamics of Northwest Iran. Geophys. J. Int. 203, 522–540. https://doi.org/10.1093/gji/ggv306.
- Goldstein, R.M., Werner, C.L., 1998. Radar interferogram filtering for geophysical applications. Geophys. Res. Lett. 25, 4035–4038.
- Gutmann, B., Weber, H., 1999. Phase unwrapping with the branch-cut method: clustering of discontinuity sources and reverse simulated annealing. Appl. Opt. 38, 5577–5593. Optica Publishing Group.
- Hastings, W.K., 1970. Monte Carlo Sampling Methods Using Markov Chains and their Applications. Oxford University Press.
- Hersbach, H., Bell, B., Berrisford, P., Hirahara, S., Horányi, A., Muñoz-Sabater, J., Nicolas, J., et al., 2020. The ERA5 global reanalysis. Q. J. R. Meteorol. Soc. 146, 1999–2049. Wiley Online Library.
- Jackson, J., McKenzie, D., 1988. The relationship between plate motions and seismic moment tensors, and the rates of active deformation in the Mediterranean and Middle East. Geophysical Journal International 93 (1), 45–73.
- Jolivet, R., Grandin, R., Lasserre, C., Doin, M.-P., Peltzer, G., 2011. Systematic InSAR tropospheric phase delay corrections from global meteorological reanalysis data. Geophys. Res. Lett. 38.
- Jónsson, S., Zebker, H., Segall, P., Amelung, F., 2002. Fault slip distribution of the 1999 M w 7.1 Hector Mine, California, earthquake, estimated from satellite radar and GPS measurements. Bull. Seismol. Soc. Am. 92, 1377–1389.
- Jordan, T.H., Sverdrup, K.A., 1981. Teleseismic location techniques and their application to earthquake clusters in the South-Central Pacific. Bull. Seismol. Soc. Am. 71, 1105–1130. http://www.bssaonline.org/content/71/4/1105.abstract.
- Karakhanian, A.S., Trifonov, V.G., Philip, H., Avagyan, A., Hessami, K., Jamali, F., Bayraktutan, M.S., Bagdassarian, H., Arakelian, S., Davtian, V., Adilkhanyan, A., 2004. Active faulting and natural hazards in Armenia, eastern Turkey and northwestern Iran. Tectonophysics 380 (3–4), 189–219.
- Karasözen, E., Nissen, E., Bergman, E.A., Ghods, A., 2019. Seismotectonics of the Zagros (Iran) from Orogen-Wide, calibrated earthquake relocations. J. Geophys. Res. Solid Earth 124, 9109–9129. https://doi.org/10.1029/2019JB017336.
- Khorrami, F., Vernant, P., Masson, F., Nilfouroushan, F., Mousavi, Z., Nankali, H., Saadat, S.A., et al., 2019. An up-to-date crustal deformation map of Iran using integrated campaign-mode and permanent GPS velocities. Geophys. J. Int. 217, 832–843. https://doi.org/10.1093/gii/ggz045.
- Kreemer, Corné, Geoffrey Blewitt, Elliot, C. Klein, 2014. A geodetic plate motion and Global Strain Rate Model. Geochem. Geophys. Geosyst. 15 (10), 3849–3889.
- Maheri-Peyrov, M., Ghods, A., Donner, S., Akbarzadeh-Aghdam, M., Sobouti, F., Motaghi, K., Hassanzadeh, M., et al., 2020. Upper crustal structure of NW Iran revealed by regional 3-D Pg velocity tomography. Geophys. J. Int. 222, 1093–1108. https://doi.org/10.1093/gji/ggaa236.
  Minson, S.E., Simons, M., Beck, J.L., 2013. Bayesian inversion for finite fault earthquake
- Minson, S.E., Simons, M., Beck, J.L., 2013. Bayesian inversion for finite fault earthquake source models I—Theory and algorithm. Geophys. J. Int. 194, 1701–1726.
- Mortezanejad, G., Rahimi, H., Romanelli, F., Panza, G.F., 2019. Lateral variation of crust and upper mantle structures in NW Iran derived from surface wave analysis.

  J. Seismol. 23, 77–108. https://doi.org/10.1007/s10950-018-9794-1.
- Nábělek, J. & Xia, G. 1995 Moment-tensor analysis using regional data: application to the 25 March, 1993, Scotts Mills, Oregon, earthquake, Geophys. Res. Lett. 22, 13–16.
- Navabpour, P., Barrier, E., 2012. Stress states in the Zagros fold-and-thrust belt from passive margin to collisional tectonic setting. Tectonophysics 581, 76–83.

- Niassarifard, M., Shabanian, E., Azad, S.S., Madanipour, S., 2021. New tectonic configuration in NW Iran: intracontinental dextral shear between NW Iran and SE Anatolia. Tectonophysics 811, 228886.
- Nissen, E., Ghods, A., Karasözen, E., Elliott, J.R., Barnhart, W.D., Bergman, E.A., Hayes, G.P., et al., 2019. The 12 November 2017 M w 7.3 Ezgeleh-Sarpolzahab (Iran) earthquake and active Tectonics of the Lurestan Arc. J. Geophys. Res. Solid Earth 124, 2124–2152. https://doi.org/10.1029/2018JB016221.
- Okada, Y., 1985. Surface deformation due to shear and tensile faults in a half-space. Bull. Seismol. Soc. Am. 75, 1135–1154.
- Rezapour, M., 2024. Aftershock analyses of the Qotur Doublet-Earthquakes on 23 February 2020 in West-Azarbaijan Province, NW Iran. Pure Appl. Geophys. 181, 37–52. https://doi.org/10.1007/s00024-023-03406-8.
- Rignot, E., Echelmeyer, K., Krabill, W., 2001. Penetration depth of interferometric synthetic-aperture radar signals in snow and ice. Geophys. Res. Lett. 28, 3501–3504. https://doi.org/10.1029/2000GL012484.
- Selçuk, A.S., Erturaç, M.K., Nomade, S., 2016. Geology of the Çaldıran Fault, Eastern Turkey: age, slip rate and implications on the characteristic slip behaviour. Tectonophysics 680, 155–173. https://doi.org/10.1016/j.tecto.2016.05.019.
- Sethanant, I., Nissen, E., Pousse-Beltran, L., Bergman, E., Pierce, I., 2023. The 2020 Mw 6.5 Monte Cristo Range, Nevada, earthquake: anatomy of a crossing-fault rupture through a region of highly distributed deformation. Bull. Seismol. Soc. Am. 113, 948–975. https://doi.org/10.1785/0120220166.
- Shabanian, E., Bellier, O., Abbassi, M.R., Siame, L., Farbod, Y., 2010. Plio-Quaternary stress states in NE Iran: Kopeh Dagh and Allah Dagh-Binalud mountain ranges. Tectonophysics 480, 280–304. https://doi.org/10.1016/j.tecto.2009.10.022.
- Storchak, D.A., Di Giacomo, D., Bondár, I., Engdahl, E.R., Harris, J., Lee, W.H.K., Villaseñor, A., et al., 2013. Public release of the ISC–GEM global instrumental earthquake catalogue (1900–2009). Seismol. Res. Lett. 84, 810–815. Seismological Society of America
- Storchak, D.A., Di Giacomo, D., Engdahl, E.R., Harris, J., Bondár, I., Lee, W.H.K., Bormann, P., et al., 2015. The ISC-GEM global instrumental earthquake catalogue (1900–2009): introduction. Phys. Earth Planet. Inter. 239, 48–63.
- Taghipour, K., Khatib, M.M., Heyhat, M., Shabanian, E., Vaezihir, A., 2018. Evidence for distributed active strike-slip faulting in NW Iran: the Maragheh and Salmas fault zones. Tectonophysics 742, 15–33.
- Taymaz, T., Ganad, A., Berberian, M., Eken, T., Iramk, S., Kapetanidis, V., Yolsal-Çevikbilen, S., et al., 2022. The 23 February 2020 Qotur-Ravian earthquake doublet at the Iranian-Turkish border: seismological and InSAR evidence for escape tectonics. Tectonophysics 229482.
- Vernant, P., Nilforoushan, F., Hatzfeld, D., Abbassi, M.R., Vigny, C., Masson, F., Nankali, H., et al., 2004. Present-day crustal deformation and plate kinematics in the Middle East constrained by GPS measurements in Iran and northern Oman. Geophys. J. Int. 157, 381–398. https://doi.org/10.1111/j.1365-246X.2004.02222.x
- Waldhauser, F., Ellsworth, W.L., 2000. A double-difference earthquake location algorithm: method and application to the Northern Hayward Fault, California. Bull. Seismol. Soc. Am. 90, 1353–1368. https://doi.org/10.1785/0120000006.
- Watson, A.R., Elliott, J.R., Lazecký, M., Mcgrath, J.D., Walters, R.J., 2024. An InSAR GNSS Velocity Field for Iran, pp. 1–13.
- Wessel, P., Luis, J.F., Uieda, L., Scharroo, R., Wobbe, F., Smith, W.H.F., Tian, D., 2019. The generic mapping tools version 6. Geochem. Geophys. Geosyst. 20, 5556–5564. https://doi.org/10.1029/2019GC008515.
- Zanjani, A., Ghods, A., Sobouti, F., Bergman, E., Mortezanejad, G., Priestley, K., Madanipour, S., et al., 2013. Seismicity in the Western coast of the South Caspian basin and the talesh mountains. Geophys. J. Int. 195, 799–814. https://doi.org/ 10.1093/gji/ggt299.
- Zarifi, Z., Nilfouroushan, F., Raeesi, M., 2014. Crustal stress map of Iran: insight from seismic and geodetic computations. Pure Appl. Geophys. 171, 1219–1236. https:// doi.org/10.1007/s00024-013-0711-9.